Preprint manuscript: submitted to Sedimentology on 17.08.2020 (Molenaar et al.)

What Controls the Remobilization and Deformation of Surficial Sediment by Seismic Shaking? Linking Lacustrine Slope Stratigraphy to Great Earthquakes in South-Central Chile

Ariana Molenaar*[1], Maarten Van Daele[2], Thomas Vandorpe[3], Gerald Degenhart[1,4], Marc De Batist[2], Roberto Urrutia[5], Mario Pino[6], Michael Strasser[1], Jasper Moernaut[1]

*__corresponding author__: ariana.molenaar@uibk.ac.at

1) Institute of Geology, University of Innsbruck, Innsbruck, Austria
2) Renard Centre of Marine Geology, Ghent University, Ghent, Belgium
3) Flanders Marine Institute (VLIZ), Oostende, Belgium
4) Medical University Innsbruck, Innsbruck, Austria
5) Faculty of Environmental Sciences & EULA-Center, University of Concepción, Barrio Universitario s/n, Concepción, Chile
6) Inst. Ciencias de la Tierra & Transdisciplinary Center for Quaternary Research in the South of Chile, Universidad Austral de Chile, Valdivia, Chile

Abstract

Remobilization and deformation of surficial subaqueous slope sediments create turbidites and soft sediment deformation structures (SSDS), which are common features in many depositional records. Paleoseismic studies have used seismically-induced turbidites and SSDS preserved in sedimentary sequences to reconstruct recurrence patterns and—in some cases—allow quantifying rupture location and magnitude of past earthquakes. However, our understanding of earthquake-triggered remobilization and deformation lacks studies targeting where these processes take place, the subaqueous slope, and involving direct comparison of sedimentary fingerprint with well-documented historical earthquakes. Here we investigate the sedimentary imprint of six megathrust earthquakes in 17 slope sediment cores from two Chilean lakes, Riñihue and Calafquén, and link it to magnitude, seismic intensity, peak ground acceleration (PGA) and Arias Intensity (I_a). Centimeter-scale stratigraphic gaps—caused by

remobilization of surficial slope sediment—were identified using high-resolution multi-proxy core correlation of slope to basin cores and six types of SSDS using high-resolution 3D X-ray computed tomography data. Centimeter-scale gaps occur at the studied sites when I_a and moment magnitude (M_w) exceed 3.85 m/s and 8.8, respectively. Total remobilization depth correlates best with I_a and is highest in both lakes for the strongest earthquakes (M_w ~9.5). In lake Riñihue, SSDS thickness and type correlates best with PGA providing first field-based evidence of progressive SSDS development with increasing PGA for SSDS caused by Kelvin-Helmholtz instability (KHI). Stratigraphic gaps occur on slope angles of ≥2.3°, whereas deformation already occurs from slope angle 0.2°. The thickness of both stratigraphic gaps and SSDS increases with slope angle suggesting that increased slope angle—and thereby gravitational shear stress—promotes both remobilization and deformation. Seismic shaking is the dominant trigger for remobilization and deformation at our studied lakes. We propose that long duration and low frequency content of seismic shaking facilitates surficial remobilization, whereas ground motion amplitude controls KHI-related SSDS development.

Keywords:

surficial remobilization, soft sediment deformation, turbidite, paleoseismology, Chilean subduction zone

1 Introduction

Turbidites and soft sediment deformation structures (SSDS) are ubiquitous within many sedimentary records (Turbidites: e.g. Bouma, 1962; Lowe, 1982; Mutti, 1992; SSDS: e.g. Lowe, 1975; Allen, 1982; Maltman, 1994). Besides triggers such as storms, tsunamis, seiches, hyperpycnal flows and rapid sediment loading, also earthquakes are considered a main cause for the formation of these sedimentary features. Several subaqueous paleoseismological studies on ocean and lacustrine sediment archives used earthquake-triggered turbidites (e.g. Goldfinger et al., 2012; Pouderoux et al., 2014; Ikehara et al., 2016; Moernaut et al., 2018) and SSDS (e.g.

Marco et al., 1996; Becker et al., 2002; Üner et al., 2019) to unravel earthquake recurrence patterns over timescales of several thousands of years. Some of these studies allowed for more specific characterization of earthquake magnitude and rupture location—and thus more quantatitive paleoseismology—by detailed investigation of spatial distribution and thickness of turbidites and SSDS (e.g. Hibsch et al., 1997; Goldfinger et al., 2012; Moernaut et al., 2014; Howarth et al., 2014; Kremer et al., 2017). To fully exploit the potential of subaqueous paleoseismic records, a thorough understanding of how different ground motion characteristics, sediment properties and slope morphologies cause and modulate remobilization and deformation of subaqueous slope sediments is paramount. Here we investigate the sedimentary imprint of remobilization and deformation of surface sediments—processes creating turbidites and SSDS—on multiple subaqueous slope sites of two Chilean lakes and correlate this to six well-documented megathrust earthquakes.

Surficial remobilization describes the earthquake-induced remolding and subsequent transportation of a thin veneer of surficial subaqueous slope sediment (Moernaut et al., 2017; McHugh et al., 2016; Schwestermann et al., 2020; McHugh et al., 2020). Surficial remobilization can transport vast amounts of sediments and particulate organic carbon from ocean margins into terminal basins (Kioka et al., 2019). The process has been proposed after the detection of i) high-turbidity bottom waters in the wake of strong earthquakes (Noguchi et al., 2012; Ashi et al., 2014), ii) strong similarities in composition of seismo-turbidites and near-surface slope sediments (e.g. McHugh et al., 2016; Moernaut et al., 2017) and iii) offsets between slope recharge rates and volume of seismically-triggered turbidites (Goldfinger et al., 2017). Moernaut et al. (2017) stated that surficial remobilization could explain the correlation of turbidite volume (or thickness) with seismic shaking intensity observed in some settings (Goldfinger et al., 2012; Moernaut et al., 2014; McHugh et al., 2016) as stronger shaking would remold deeper into the sediment resulting in higher turbidite volume. Therefore, seismically-

induced surficial remobilization might allow for quantification of paleoseismic intensity through the analysis of thickness of seismo-turbidites.

Most existing studies inferred surficial remobilization by studying the resulting deposits in the ocean trenches or lacustrine basin floors (i.e. turbidites). However, turbidite composition is influenced by a wide range of processes during remobilization, transport and deposition, such as incorporation into the turbidity current of additional sediments through landslide processes and turbidity current erosion or post-depositional alteration of chemical composition through redox reactions or radioactive decay. All these factors can introduce bias to the interpretation of the underlying remobilization process using turbidite records (Schwestermann et al., 2020). Recently, surficial remobilization was stratigraphically detected on a Japan Trench slope (2.5° slope angle) in form of three centimeter-scale gaps that were temporally linked to the three strongest (M_w >8) historical earthquakes in that region (Molenaar et al., 2019). However, one slope site does not suffice to evaluate the modulating effect of morphology (e.g. slope angle or slope orientation) on surficial remobilization or the spatial extent of centimeter-scale gaps over extensive slope areas.

SSDS form when sediment strength is reduced through sudden increase of pore pressure facilitating hydroplastic deformation, liquefaction or even fluidization with increasing pore pressure to grain weight ratio (Knipe, 1986; Ortner, 2007). Stresses caused by gravity or inversed density gradients (i.e. Rayleigh-Taylor Instability) are insufficient to induce deformation during stable conditions, but drive deformation when sediment is sufficiently weakened (Owen et al., 2011). Also, earthquake-induced shear stress at layer interfaces can induce deformation (i.e. Kelvin-Helmholtz Instability (KHI); Heifetz et al. (2005). Resulting SSDS have been linked to seismic shaking in many onshore and offshore settings—both contemporaneous and paleo—and used to investigate paleo-earthquakes and unravel earthquake recurrence patterns (e.g. Marco et al., 1996; Becker et al., 2002; Monecke et al.,

2004; Obermeier, 2009; Avşar et al., 2016; Lu et al., 2017). Previous studies opened up the possibility to derive quantitative earthquake information from subaqueous sedimentary records by correlating shaking intensity with specific characteristics of lacustrine SSDS, such as thickness (e.g. Hibsch et al., 1997; Rodrıguez-Pascua et al., 2003) or type (e.g. Sims, 1973; Rodríguez-Pascua et al., 2010).

Most of these studies focused on SSDS related to prehistorical earthquakes on outcrops of paleo-lakes (e.g. Marco et al., 1996; Rodríguez-Pascua et al., 2010)—which inhibits validation of estimated ground motion parameters or magnitude of the causative paleo-earthquakes—or identified SSDS using 2D images of a small amount of sediment cores (e.g. Monecke et al., 2004; Avşar et al., 2016)—which potentially leaves small-scale features undetected and hinders the evaluation of spatial SSDS variability.

Our understanding of the impact of earthquakes on subaqueous sediments lacks detailed investigation on where these processes take place: the subaqueous slopes. Also, to thoroughly evaluate relationships between observed sedimentary imprint and ground motion characteristics, we need accurate correlation of earthquake-related sedimentary imprint to well-documented historical earthquakes. Here we target a total of 17 slope sites in two Chilean lakes—Riñihue and Calafquén—and compare the sedimentary sequences to accurately-dated turbidite records from the basin floors in these lakes related to five historical and one prehistorical megathrust earthquake with variable rupture modes and magnitudes (Moernaut et al., 2014). We investigate surficial remobilization by identifying centimeter-scale gaps using detailed multi-proxy correlation of slope cores to these basin seismo-turbidite records, and deformation using high-resolution X-ray computed tomography (CT) data to resolve SSDS in 3D.

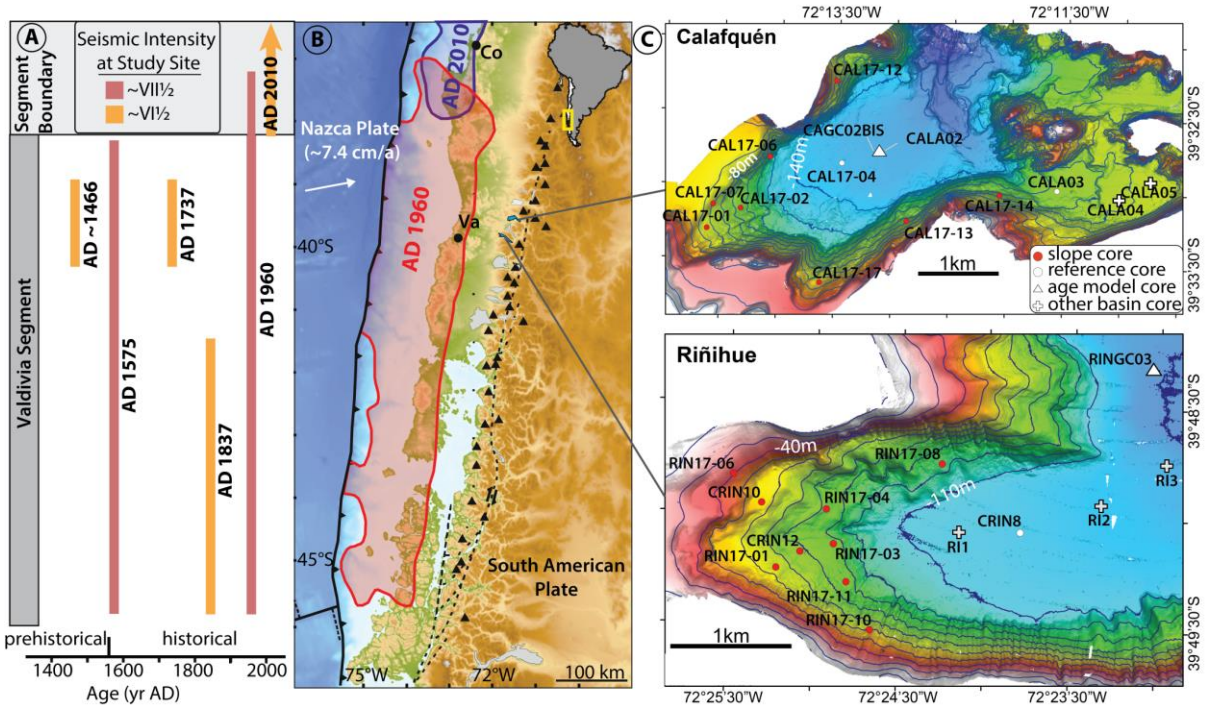

Figure 1 (A) The South-Central Chilean subduction zone (Valdivia segment and southern extremity of the Maule segment) and rupture extent of the six studied megathrust earthquakes based on historical and paleoseismic data (Moernaut et al., 2014; Wils et al., submitted). (B) Tectonic setting of our study sites and rupture areas (> 5 m coseismic slip) of the AD1960 and the AD2010 earthquakes (Moreno et al., 2009; Moreno et al., 2012, respectively). Triangles depict volcanoes and dashed lines active fault systems. Subfigure and B are adapted from Moernaut et al. (2018). (C) Bathymetric maps of the studied basins of lake Calafquén (Moernaut et al., 2019) and lake Riñihue (this study) along with the locations of slope cores and reference basin cores as well as previously published basin cores (Moernaut et al., 2014; Van Daele et al., 2014). Full lake bathymetry in Figure S1 and S2 of the supporting information.

2 Setting

2.1 Regional Earthquake History and Seismic Intensities

Lakes Riñihue and Calafquén are located between 39.5°S and 40°S in South-Central Chile, which is tectonically dominated by the subduction of the Nazca Plate below the South American Plate with a convergence rate of ~7.4 cm/a (DeMets et al. (2010); Figure 1). The subduction zone megathrust divides at around 37.5-38.5°S into two major seismotectonic segments, the southern Valdivia segment and the northern Maule segment (Métois et al., 2012), both capable of generating giant (M_w>8.5) earthquakes. The Maule segment generated the M_w 8.8 AD 2010 earthquake and the Valdivia segment the M_w 9.5 AD 1960 earthquake—the strongest earthquake ever recorded. At the Valdivia segment, historical documents describe

three other strong historical megathrust earthquakes in AD 1837, AD 1737 and AD 1575 (Lomnitz, 1970; Cisternas et al., 2005). Another prehistorical earthquake in AD ~1466± 4 was identified and accurately dated based on seismo-turbidite records in lakes Riñihue and Calafquén (Moernaut et al., 2014).

For the AD 2010 earthquake, Modified Mercalli Intensities (MMI) at both lakes were estimated based on witness reports as VI$^{1}/_{2}$ at lake Calafquén and VI$^{1}/_{4}$ at lake Riñihue (U.S. Geological Survey, 2020; Moernaut et al., 2014). For the AD 1960 earthquake, seismic intensity was estimated using the Medvedev-Sponheuer-Karnik (MSK) scale as VII$^{1}/_{2}$ at both lakes (Lazo, 2008; Moernaut et al., 2014). For these intensity levels, the MMI and MSK scales give roughly equivalent values (Musson et al., 2010). Accordingly, we use the general term "seismic intensity" to refer to both scales. Seismic intensity of the other four megathrust earthquakes were estimated by comparing the cumulative thickness of seismo-turbidites relative to the AD 1960 and AD 2010-related turbidite (Moernaut et al., 2014). This results in VII$^{1}/_{2}$ for the AD 1575 earthquake and VI$^{1}/_{2}$ for the AD 1837, AD 1737 and AD ~1466 earthquakes.

Historical reports suggest that the AD 1575 earthquake rupture was of similar size as the AD 1960 earthquake (Cisternas et al., 2005) as this earthquake also caused a large tsunami, a similar pattern of coastal uplift/subsidence, triggered large onshore landslides and a seismo-turbidite as far south as Aysén Fjord (~45°S) (Wils et al., submitted). Therefore, the AD 1575 earthquake, as the AD 1960 earthquake, has been interpreted as resulting from a full rupture of the Valdivia segment and can be estimated to a magnitude of M_w ~9.5. The AD 1837 and AD 1737 earthquakes had lower magnitudes of M_w ~9 (Moernaut et al., 2014; Cisternas et al., 2017) and M_w ~7.7 (Lomnitz, 1970), respectively. The AD 1837 earthquake, which caused a large transpacific tsunami, ruptured at a wide range of depth along the southern half of the Valdivia segment (Cisternas et al., 2017). The AD 1737 earthquake, which did not cause a large tsunami,

is considered to be a deep partial rupture at the northern third of the segment (Cisternas et al., 2017). Based on similar turbidite imprint and no conclusive evidence of a tsunami or coseismic coastal elevation changes, Moernaut et al. (2014) linked the prehistorical AD ~1466 earthquake to a similar rupture location and size as the AD 1737 earthquake.

Long cores, which covered the last 3.5-4.7 kyrs in both lakes, allowed to resolve a recurrence rate of ~292 and ~139 years for earthquakes with seismic intensity of VII$^{1}/_{2}$–similar to the AD 1960 earthquake—and VI$^{1}/_{2}$, respectively(Moernaut et al., 2018).

2.2 Lake Setting and Sedimentology

Lakes Riñihue and Calafquén are glacigenic lakes located at the foot of the volcanically active Andes along the northern third of the Valdivia segment (Figure 1 and Figure S1 and S2 in the supporting information). Lakes Riñihue and Calafquén have a size of 28 km x 2-4 km and 24 x 2-6 km and maximum depth of 323 m and 212 m, respectively. Both lakes are oligotrophic and monomictic with mixing during winter (Campos, 1984). The thermocline in both lakes develops from late spring to autumn from ~20 to ~40 m (Campos, 1984; Campos et al., 2001). No large (>5 m) lake level fluctuations have been reported in historic records, aside from the damming of lake Riñihue's outflow after the AD 1960 earthquake (Campos, 1984).

The background sediment (i.e. formed during steady-state sedimentation under normal conditions) of both lakes consists of mm-scale biogenic varve couplets of diatomaceous ooze related to diatom blooms during spring and clay-to-silt sized organic-rich terrestrial material related to increased run-off during winter (Van Daele et al., 2014). Background sedimentation rates based on varve counting are ~1 mm/a in both lakes (Moernaut et al., 2014).

Thin (up to ~1 cm) volcanic deposits are embedded in the background sediment and consist of tephra air-fall deposits and lahar deposits related to volcanic eruptions of nearby volcanoes at the eastern end of the lakes (Van Daele et al., 2014). Tephra layers are black coarse-grained deposits corresponding to peaks in magnetic susceptibility and have been used

as chronostratigraphic markers using their geochemical fingerprints (Moernaut et al., 2014; Van Daele et al., 2014; Fontijn et al., 2016). Lahar deposits in the studied basins are light beige or light gray fine-grained deposits also corresponding to elevated magnetic susceptibility although less pronounced than the tephra fall deposits. The thickness and grainsize of the lahar deposits depends on proximity to the lahar inflow and water depth of the core location as fined-grained volcanic material is mainly transported by over- or interflows (Van Daele et al., 2014).

Fine-grained turbidites within the studied basins have been linked to six strong megathrust earthquakes (i.e. AD 2010, AD 1960, AD 1837, AD 1737, AD 1575 and AD ~1466; Moernaut et al. (2014)) through accurate dating by varve counting, xs^{210}Pb/^{137}Cs radionuclide data as well as tephrochronology (Moernaut et al., 2014; Van Daele et al., 2014). Turbidites have a visually homogenous appearance often with a thin coarse-grained base and thin clay cap (Moernaut et al., 2014). Commonly, magnetic susceptibility decreases upwards within the turbidite as coarse-grained bases consist mainly of reworked tephra with elevated magnetic susceptibility values. Intralake correlation of basinal cores and correlation to the eruptive history of Villarrica Volcano shows that erosion at the core sites by these fine-grained seismo-turbidites is negligible (Moernaut et al., 2014; Van Daele et al., 2014).

Our study focusses on the slopes of three subbasins in the western shallower part of both lakes (one in lake Riñihue and two in lake Calafquén, see Figure S1 and S2 in the supporting information), sheltered from any major river or lahar inflows to exclude turbidites or erosion related to flood-induced hyperpycnal flows or the proximal, coarse-grained fraction of lahars. We cored sites in a wide range of water depths (39-113 m and 65-144 m in lake Riñihue and lake Calafquén, respectively), slope gradients (0.2-9.5° and 0.2-14.2° in lake Riñihue and lake Calafquén, respectively) and slope aspects to compare the effect of megathrust earthquakes with different rupture characteristics and magnitude on slope sites with varying morphology. Sites were chosen on relatively smooth slope morphology away from

gullies and at a minimum depth of 39 m to avoid erosion by surface currents and wave action. A water depth that is the same or deeper than the thermocline also allows for deposition of fine-grained lahar material by interflows (Van Daele et al., 2014) and preservation of mm-scale lamination essential for stratigraphic correlation.

3 Methods

3.1 Multibeam Bathymetry

Multibeam bathymetry of both lakes was acquired in December 2017 using a Norbit WMBS system, combined with an SGR6 (positioning, decimeter horizontal accuracy) and SBD-IMU-S2 (roll, pitch and azimuth at <0.02° accuracy). During the survey, pulse frequency as well as swath direction and angle were adapted according to water depth and bottom morphology. Raw data was acquired using QINSy, while processing (sound velocity correction and spike removal) of the data was done using Qimera. The bathymetric maps presented in our study and used for slope angle analysis have a horizontal grid cell size of 2 m. The slope angle of each study site was determined by computing the maximum slope angle at a center cell based on its 8 immediate neighboring cells using the slope tool from the spatial analyst toolbox in ArcGIS 10.6. For basin sites—where ArcGIS raster-derived slope angles were inaccurate due to noise within the bathymetric data—slope angles were determined over a 15 meters cross-section perpendicular to the contour lines using Global Mapper 13. To account for possible inaccuracy due to GPS uncertainty, vessel movement, a non-vertical rope during coring or noise in the bathymetric data, the slope angle over a 12, 20 and 50 meters cross-section perpendicular to the contour lines was measured and used to calculate a maximum and minimum deviation from the ArcGIS-derived slope angle.

3.2 Sediment Cores

Sediment cores were taken in December 2017 using a percussion-driven UWITEC gravity corer. Before opening, X-ray computed tomography (CT) scans were taken with a

Siemens Somatom Definition Flash at Ghent University hospital with a 0.13×0.13×0.30 mm resolution. CT scans of cores CRIN8, CRIN12, CRIN10 and CALA03 were made at the Medical University Innsbruck using a Siemens Somatom Definition AS with 0.20×0.20×0.30 mm resolution. A section of ~30 cm of RIN17-11 was cut and µCT-scanned at a resolution of 0.06×0.06×0.06 mm using a Scanco Medical XtremeCT II at the Medical University of Innsbruck. Gammy density of closed cores was measured (0.5 cm step-size) using a GEOTEK Multi-Sensor Core Logger (MSCL) of the Austrian Core Facility (University of Innsbruck). After core opening, white-calibrated images were taken using a Smartcube Camera Image Scanner and magnetic susceptibility was measured (0.2 cm step-size) using the GEOTEK MSCL equipped with a BARTINGTON MS2E surface sensor. Visual contrast and color variability of the pictures were enhanced using the histogram equalization function in Corel Photo Paint 2018. This function spreads the most frequent values on the colour intensity histogram generating non-natural colours to enhance colour variation. Additional non-white-calibrated images were made using the camera of an ITRAX XRF core scanner with polarizing filter to reduce glare of the wet sediment surface. SSDS were detected and visualized on CT scan data using both FIJI (FIJI is just ImageJ) (Schindelin et al., 2012) and VolumeGraphics VGStudio 3.3.

3.3 Calculation of Ground Motion Parameters

Peak Ground Acceleration (PGA) and Arias Intensity (I_a) at the studied lake basins were calculated using ground motion prediction equations developed for the Chilean subduction zone (Idini et al. (2017) and Céspedes et al. (2019), respectively). These calculated ground motion parameters were used only for relative comparison as the rupture location, extent and depth of the historical and prehistorical AD ~1466 earthquakes have large uncertainties. Also, formulas consider maximum magnitudes of M_w 8.8 (i.e. AD 2010 earthquake), making calculated values for the M_w ~9.5 AD 1960 and AD 1575 earthquakes less reliable. Both

formulas use shortest distance to the rupture area, magnitude and shear wave velocity in the upper 30 m. Calculation of I_a also considers hypocentral depth.

The shortest distance from each lake to the fault rupture was calculated by Pythagoras' theorem using the shortest horizontal distance to the rupture area and the estimated depth of the megathrust seismogenic zone at this location based on Tassara et al. (2006). For the AD 2010 earthquake, closest horizontal distance was taken at 38.07°S, 72.87°W (Moernaut et al. (2014), 195 km and 170 km for lake Riñihue and lake Calafquén, respectively), and a depth of 49 km. For the AD 1960, AD 1575, AD 1737 and AD ~1466 earthquakes, a horizontal distance was considered to 39.5°S, 72.9°W, east of Valdivia (i.e. 50 km for both lakes), and rupture area depth of 31 km. For the southern AD 1837 earthquake, closest horizontal distance was taken close at the ocean inflow of the Río Maullín (Moernaut et al., 2014) at 41.51°, S 73.49°W (210 km and 240 km for lake Riñihue and lake Calafquén, respectively), and rupture depth at 28 km.

Hypocentral depths of the AD 2010 and AD 1960 earthquakes were taken as 34 km (Nelson Pulido et al., 2011) and 30 km (Cifuentes, 1989; Krawcyzk, 2003), respectively. As an approximation, hypocentral depths for the other earthquakes were also taken as 30 km as they ruptured the same segment as the AD 1960 earthquake.

The average shear wave velocity in the uppermost 30 m of sediment was estimated at 200 m/s, which is a value characteristic for soft soils (Ambraseys et al., 1996).

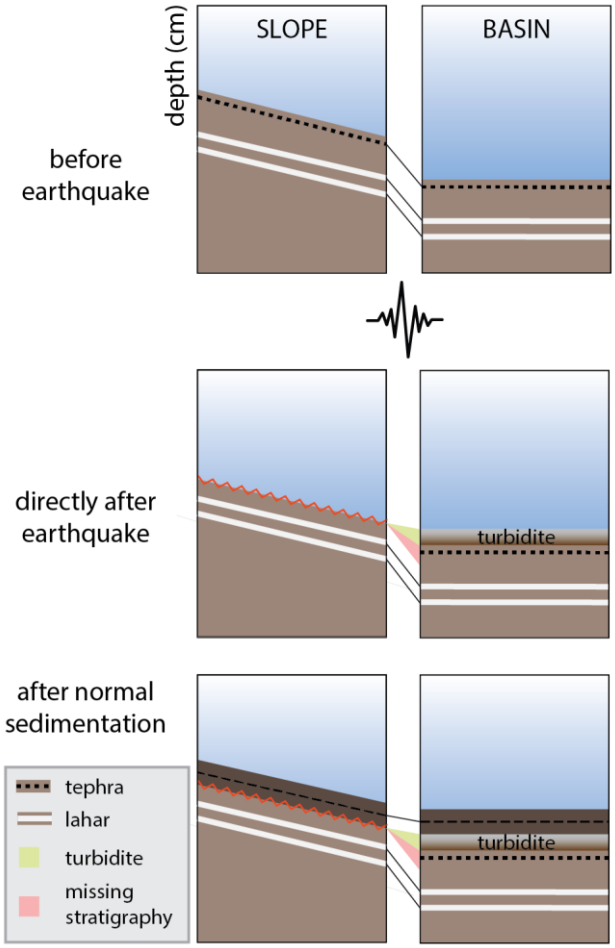

Figure 2 Representation of a slope and basin sequence in three situations: before and directly after an earthquake as well as after another period of "normal" post-event sedimentation. Normal sedimentation includes hemipelagic sedimentation intercalated by tephra and lahar deposits.

3.4 Surficial Remobilization: Detecting and Quantifying Centimeter-Scale Gaps

We propose stratigraphic correlation of slope sequences with continuous basin sedimentary sequences as a tool to detect centimeter-scale gaps potentially caused by surficial remobilization. Gaps are linked to a seismo-turbidite record within the aforementioned basin core to infer whether these gaps were caused by one of the six megathrust earthquakes.

Our assumption is that during an earthquake, the uppermost sediment is eroded from the slope, transported to the basin and deposited as a turbidite (Figure 2). After the event, normal sedimentation resumes both on the slope and in the basin creating a gap within the slope sequence exactly at the stratigraphic level of the causative earthquake. We hypothesize that sediment lithology and sedimentation rate on the slope and in the basin are highly comparable

301 if i) the study locations are sheltered from major river inlets; ii) are at or below the thermocline
302 to allow for sedimentation by interflows; and iii) erosion by turbidites at the basin locations is
303 negligible.

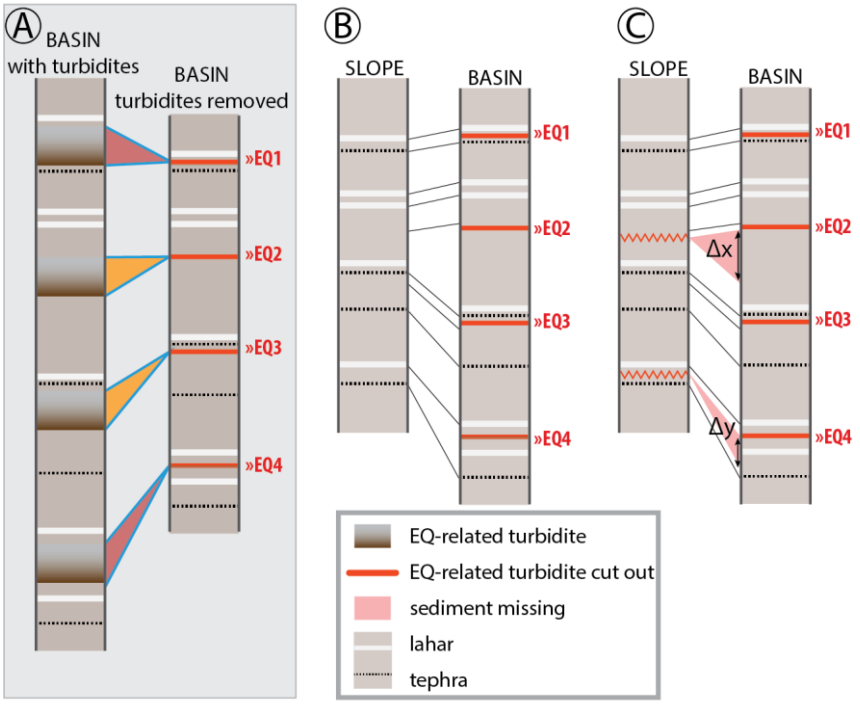

304

305 *Figure 3) (A) Turbidites are linked to a seismo-turbidite record (Moernaut et al., 2014) and then visually*
306 *removed from the basin sequence (red line = earthquake marker); (B), (C) centimeters-scale gaps are identified*
307 *and linked to earthquake markers by correlation of a slope sequence to the reference basin sequence without*
308 *turbidites. Remobilization depth is quantified by measuring the thickness of the missing sediment from the basin*
309 *sequence (Δx cm and Δy cm).*

310 First, turbidites within a reference basin core are correlated to a seismo-turbidite record
311 as presented by Moernaut et al. (2014) (supporting information Figure S3 and S4). Then, to
312 represent a continuous sediment sequence for visual correlations, earthquake-triggered
313 turbidites are cut from the reference basin sequences and their stratigraphic location marked as
314 `earthquake markers` (Figure 3a). Next, the slope sequence is correlated to the corresponding
315 basin sequence by distinct non-seismic marker layers and trends (e.g. tephras, lahar deposits,
316 and variations in magnetic susceptibility or color) constraining the stratigraphic location of the
317 earthquake marker in the slope sequence by correlating directly above and below this horizon
318 (Figure 3b). Core correlation is based on images (e.g. optical images, CT images) and high-

resolution scanning data (e.g. magnetic susceptibility), resolving small-scale changes in sediment lithology. Finally, gaps are identified in the slope sequence by detecting sediment sections that are present in the basin sequence but not in the slope sequence (Figure 3c). The amount of remobilization is quantified in centimeters by measuring the thickness of the missing sediment section represented by the basin sequence (Δx and Δy in Figure 3c). Lahar deposit thickness strongly depends on water depth, due to deposition by interflows, and distance to the lahar inflow point (Van Daele et al., 2014). If the thickness of lahar deposits in the studied slope core varies significantly with those in the basin core, remobilization depth is determined from correlation to an intact slope core of comparable water depth.

3.5 Types of Sediment Deformation Structures

Based on literature, the observed SSDS are subdivided into six types: i) disturbed lamination, ii) folds, iii) intraclast breccia, iv) faults, v) load structures and vi) injection structures. We distinguish between SSDS intervals, which are continuous sections of deformed sediment, and SSDS types as intervals can contain several types of SSDS.

Disturbed lamination involves undulation or thickening and thinning over several laminations without loss of the laminations' lateral continuity (Rodríguez-Pascua et al., 2000). Folds describe SSDS where laminations are folded and have a clear vergence. Intraclast breccias are sections of homogenized background sediment comprising fragments of laminations. An intraclast breccia always has a sharp contact to the overlying lamina, but the basal contact can be gradual (Agnon et al., 2006). Normal faults involve brittle deformation of sediment and formation of small-scale faults. Load structures evolve when overlying sediment sinks into underlying sediment and are mainly driven by inverse density gradients (i.e. denser sediment on top) (Owen, 2003). Injection structures form when sediment penetrates into the overlying sediment as pore pressure exceeds lithostatic stress and tensile strength of the overlying sediment (Jolly and Lonergan, 2002).

Coring disturbance can also cause SSDS as i) friction at the liner creates domical shapes; ii) collapse of sediment into gas cracks results in symmetric normal faults and iii) on-deck core sealing shortly after core acquisition can disturb the top-most sediment (Jutzeler et al., 2014). Therefore, circular-symmetrical SSDS; large cylindric sections of normal faults and disturbed laminations at the core top are interpreted as coring disturbance and excluded from our analysis.

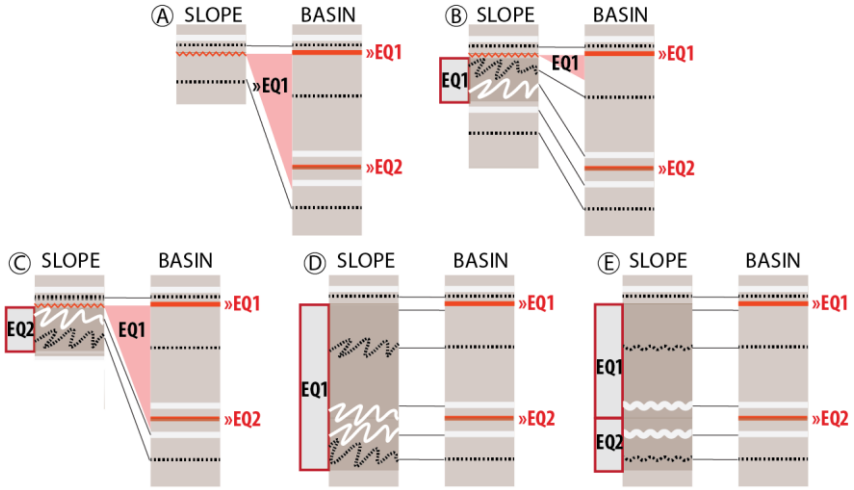

Figure 4 Examples of our correlation strategy when centimeter-scale gaps or SSDS cover the stratigraphical level of multiple earthquake markers. (A) centimeter-scale gap covering two earthquake markers; (B) centimeter-scale gap and SSDS correlating to one earthquake marker; (C) centimeter-scale gap covering two earthquake markers and SSDS; (D) SSDS covering two earthquake markers that deformed the older earthquake marker; (E) SSDS covering two earthquake markers that did not clearly deform the older earthquake marker.

3.6 Linking Sedimentary Imprint to the Six Megathrust Earthquakes

Centimeter-scale gaps are linked to one of the six megathrust earthquakes if correlation lines above and below the gap are also above and below an earthquake marker within the basin sequence. For SSDS intervals, we propose one of the six megathrust earthquakes as a trigger if the top of the SSDS interval is within 2 cm below the stratigraphic level of an earthquake, as uppermost sediments are most susceptible to seismically-induced deformation (Sims, 1973; Marco et al., 1996; Monecke et al., 2004; Avşar et al., 2016).

Assumptions must be made when SSDS or gaps cover the stratigraphic level of multiple earthquake markers. In case a centimeter-scale gap eroded the stratigraphic depth of two

earthquake markers, it is assigned entirely to the younger earthquake (Figure 4a). If a SSDS occurs below a gap, the SSDS is correlated to the same earthquake that generated the gap (Figure 4b) unless the stratigraphic level of another earthquake marker is eroded. In that case, it is verified whether the SSDS was within 2 cm of the sediment-water interface during the older earthquake and the SSDS is correlated to the older event (Figure 4c). If a SSDS interval covers two earthquake markers within the basin sequence and the stratigraphic level of the older earthquake is clearly deformed—for example with folds or load structures—the SSDS is assigned entirely to the youngest earthquake (Figure 4d). If a SSDS interval covers two earthquake markers, but the stratigraphic level of the older earthquake is not clearly deformed—for example with disturbed lamination—the SSDS interval is split and assigned to both earthquakes (Figure 4e). The possible effects of these scenarios are discussed in section 5.1.

Table 1 A summary of earthquake-related sedimentary imprint in form of i) centimeter-scale gaps represented by remob. (cm) in table; ii) SSDS thickness represented by deform. (cm) in table and iii) SSDS type (DL: Disturbed Lamination; Fo: Folds; IB: Intraclast Breccia; Fa: Faults; LS: Load Structure; IS: Injection Structure). We display sedimentary imprint both per core and per earthquake (i.e. the six megathrust earthquakes). Deformation by the AD2010 earthquake is not considered due to possible coring disturbance of top sediment.

	AD2010			AD 1960			AD 1837			AD 1737			AD 1575			AD ~1466				
Lake Calafquén	remob (cm)	deform (cm)	SSDS type	remob (cm)	deform (cm)	SSDS type	remob (cm)	deform (cm)	SSDS type	remob (cm)	deform (cm)	SSDS type	remob (cm)	deform (cm)	SSDS type	remob (cm)	deform (cm)	SSDS type	Total remob. per core (cm)	Total deform. per core(cm)
CALA03																			0	0
CAL17-04																			0	0
CAL17-01																			0	0
CAL17-02				6															6	0
CAL17-06	3			6							4	DL	12	2	LS		3	DL	21	9
CAL17-07	13							3	DL		6	Fo					14	DL, Fo	13	23
CAL17-12														2	LS				0	2
CAL17-13				3															3	0
CAL17-14				7							10	DL, Fo	16				8	DL	23	18
CAL17-17				2							6	DL							2	6
Total per Lake (cm)	16	-		24	0		0	3		0	26		28	4		0	32		68	58
Lake Riñihue	remob (cm)	deform (cm)	SSDS type	remob (cm)	deform (cm)	SSDS type	remob (cm)	deform (cm)	SSDS type	remob (cm)	deform (cm)	SSDS type	remob (cm)	deform (cm)	SSDS type	remob (cm)	deform (cm)	SSDS type	Total remob. per core (cm)	Total deform. per core(cm)
CRIN8														1	IB				0	1
CRIN10														2	IB				0	2
CRIN12				6				2	DL					1	IB				6	3
RIN17-01				20							13	DL, LS, IS	2	1	DL				22	14
RIN17-03					3	DL								6	Fa				0	9
RIN17-04					4	DL	6				3	DL	5	5	LS		8	DL	11	20
RIN17-06				5	7	Fo		4	DL										5	11
RIN17-08				5	5	DL, Fo	6	1	IB		2	Fo	1						12	8
RIN17-10				6	8	Fo							14						20	8
RIN17-11				1	25	Fo							4	8	IB				5	33
Total per Lake (cm)	0	-		43	52		12	7		0	18		26	24		0	8		81	109
Total per EQ (cm)	16			67	52		12	10		0	44		54	28		0	40		149	167

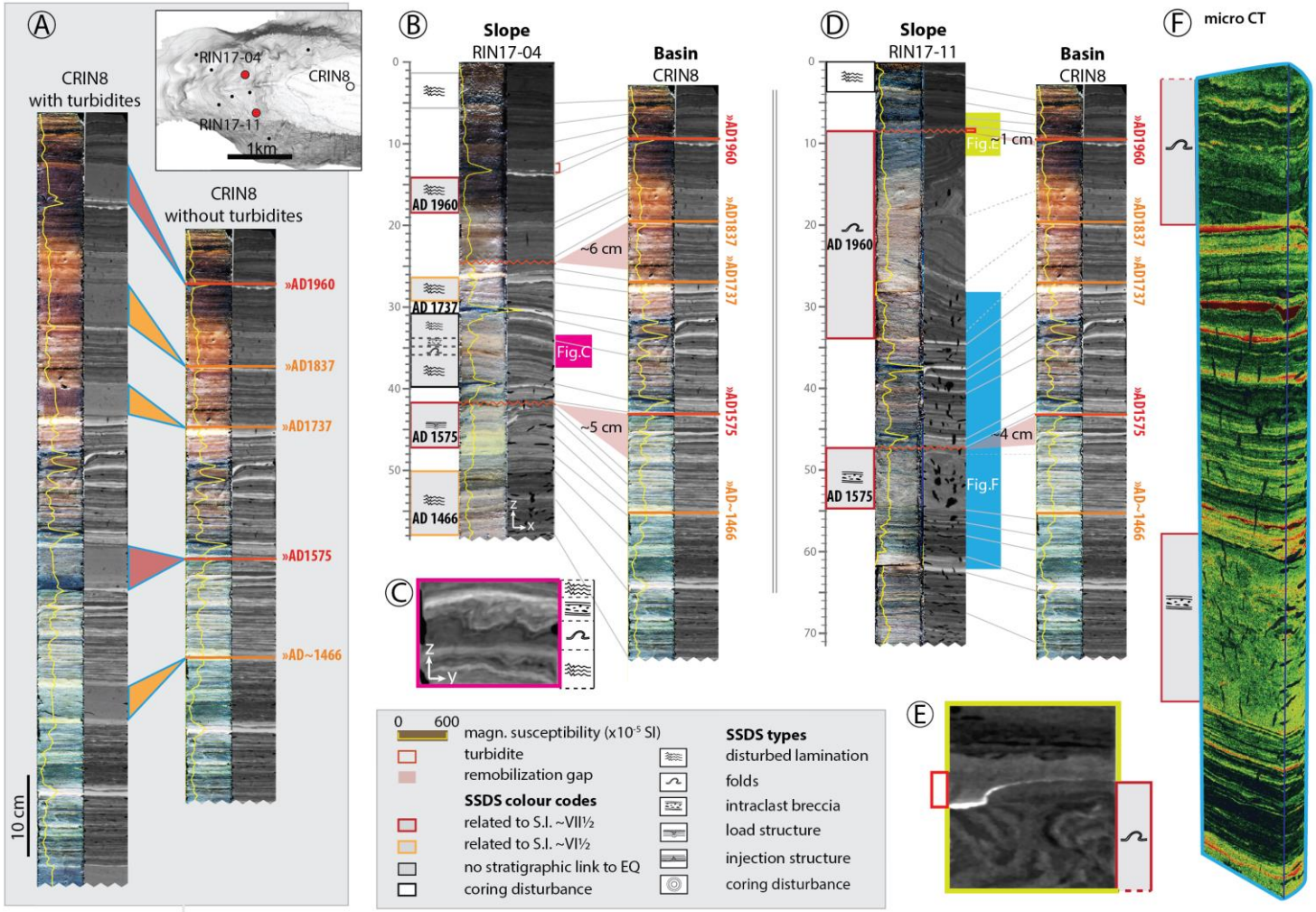

Figure 5 (A) Reference basin core with and without turbidites of lake Riñihue. (B) and (D) Two examples of slope-to-basin core correlation and SSDS identification. The three images depict (C) a SSDS displayed in a CT cross section perpendicular (yz-view) to the orientation of the main CT image (xz-view); (E) CT image of the AD 1960 turbidite and (F) micro-CT image of RIN17-11. Micro-CT color scale from dark green (low radiodensity) to red (high radiodensity). All correlations of lake Riñihue are located in Figure S6-S8 of the supporting information.

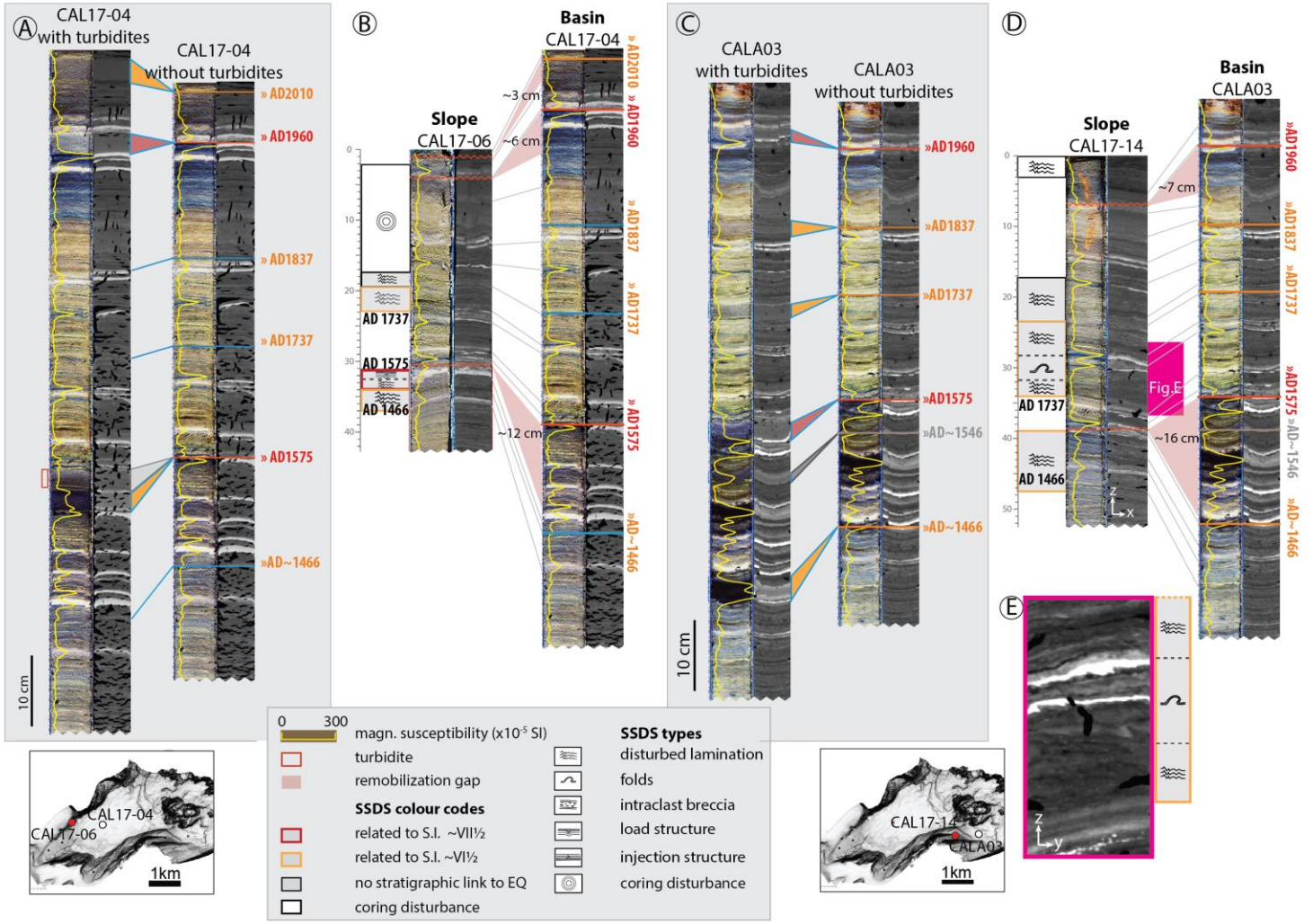

Figure 6 Reference basin cores with and without turbidites for the eastern (A) and western (C) basin of lake Calafquén along with examples of slope-to-basin core correlation and SSDS identification (B) and (D). (E) A SSDS displayed in CT cross section perpendicular (yz-view) to the orientation of the main CT image (xz-view). All correlations of lake Calafquén are located in Figure S9-S11 of the supporting information.

4 Results

4.1 Centimeter-Scale Gaps and SSDS in Lake Riñihue and Lake Calafquén

4.1.1 Centimeter-Scale Gaps

In the lake Riñihue cores, 13 gaps were identified in 9 slope sequences with remobilization depths ranging from 1 to 20 cm and average remobilization depth of 6.2 cm (Table 1, Figure 5 and supporting information Figure S6-S8 for all correlations). Undeformed slope sequence thicknesses above or below centimeter-scale gaps are averagely 94% of the reference basin sequence suggesting similar sedimentation rates on slopes and in the basin.

Thin gravity flow deposits (~1 cm) occur in slope cores for the AD 1960 (RIN17-03, RIN17-04, RIN17-08, RIN17-10, RIN17-11) and AD 1575 (RIN17-01, RIN17-03 and RIN17-10) earthquakes. We interpret these event deposits as turbidites sourced from the higher slope based on their homogenous appearance and thin sandy base in some cases. A thicker gravity flow deposit (3.5 cm) in RIN17-01 contains lamination fragments indicating a relatively short transport distance compared to the more homogeneous turbidites (supporting information Figure S6).

In the lake Calafquén cores, 9 gaps were identified in 8 slope sequences with remobilization depths ranging from 2 to 16 cm and average remobilization thickness of 7.6 cm (Table 1; Figure 6 and supporting information Figure S9-S11 for all correlations). Undeformed slope sequence thicknesses above or below centimeter-scale gaps are averagely 92% of the reference basin sequence. In CAL17-17 and CAL17-07 (water depth 65 m and 79 m, respectively), the organic-rich upper layer and the lahar deposits directly above and below the stratigraphic level of the AD1960 earthquake are less thick than in the deeper basin reference core. Therefore, intact slope core CAL17-01 of similar water depth (76 m) was used as reference to determine remobilization depths for the AD 1960 gaps in CAL17-17 and CAL17-07 (Figure S9 and S10 in the supporting information).

Thin (<1 cm) AD 1960 turbidites occur in slope cores CAL17-02 and CAL17-17 which consist of a homogenous layer with a base of reworked tephra and a AD1575 turbidite in CAL17-01 and CAL17-02.

Cores CAL17-04 and CALA03 were selected as basin reference cores for the western and eastern basin, respectively (Figure 6a and c). Aside from turbidites related to the six megathrust earthquakes, CALA03 also includes a single turbidite that is not present in any other basin of Lake Riñihue or Lake Calafquén and dated to AD 1546 most likely caused by a local earthquake (Moernaut et al., 2014). In CAL17-04, another turbidite is located directly above the AD 1575 earthquake with few laminations separating both turbidites. These turbidites are also cut from the basin stratigraphy for comparison to slope sequences.

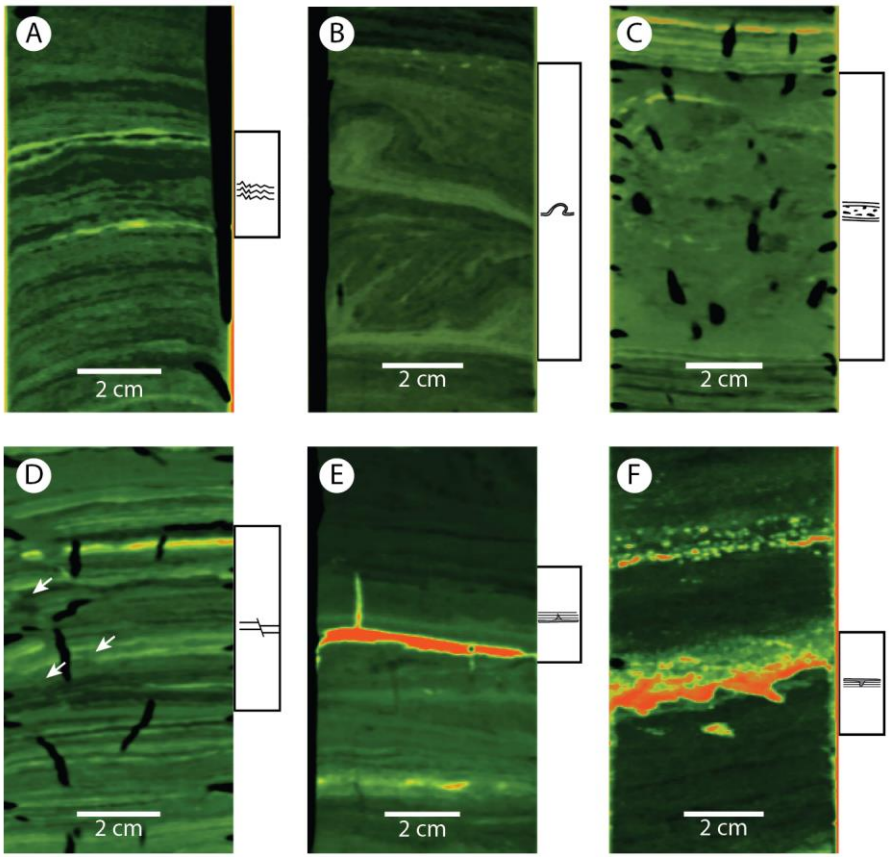

Figure 7 Characteristic examples of the six SSDS types observed in lake Riñihue and Calafquén obtained from medical CT data (radiodensity: dark green: low; yellow to red: high). (A) Disturbed lamination, (B) folds (arrows point out offset), (C) intraclast breccia, (D) faults, (E) injection structures, (F) load structures. We adapted the color scale for each SSDS to optimize visualization. Black cracks are caused by degassing of the sediment core.

Preprint manuscript: submitted to Sedimentology on 17.08.2020 (Molenaar et al.)

4.1.2 Soft Sediment Deformation Structures

The studied cores of lakes Riñihue and Calafquén contain a total of 31 and 18 SSDS intervals, respectively. Of these SSDS intervals, 20 in lake Riñihue (i.e. 65% of total) stratigraphically link to one of the six megathrust earthquakes and 10 in lake Calafquén (i.e. 56% of total; Table 1). From the 19 SSDS intervals that do not correlate within 2 cm of an earthquake marker, 10 are located above (i.e. within 1 cm) or in a lahar deposit and four above a tephra layer.

Intraclast breccias are compared with the corresponding section in the basin sequence to distinguish them from gravity flow deposits. Intraclast breccia thickness compares to thickness of the undisturbed basin sequence as they result from in-situ deformation or only involve very little transportation. Also, intraclast breccia contain clasts of laminations or dispersed high-density of which the position stratigraphically correlates to the undisturbed basin sequence. Gravity flow deposits also consist of background sediment, but are either homogenous due to breaking of laminae by transport in a turbulent flow (i.e. turbidites) or the original position of lamination fragments is lost during transportation (see RIN17-01 in Figure S6 of the supporting information). Also, thickness of gravity flow deposits can be much different than corresponding remobilization depths on the slope (Figure 5 and Figure 6).

Cores of lake Riñihue contain all six SSDS types, whereas cores of lake Calafquén are dominated by disturbed lamination and three occurrences of folds (Figure 7 and Table 1). Load and injection structures are scarce with only one injection structure (RIN17-01) and three load structures (one in lake Riñihue and two in lake Calafquén). Two faults are identified in the lake Riñihue cores: one in RIN17-03, which correlates to the AD 1575 earthquake marker (Figure 7d and Figure S6 in the supporting information), and another in CRIN8, which does not correlate to an earthquake marker (Figure S5 in the supporting information).

Gas cracks hindered detection of SSDS (especially disturbed lamination and intraclast breccia) in the lower part of cores CAL17-01, CAL17-02, CAL17-17, CAL17-04 and RIN17-06. However, if present, we expect folds, load structures and injection structures to still be detectable in sediment cores with gas cracks as this involves clear bending and vergence of layers or high-density layers. Also, cores CAL17-12 and CAL17-06 contain severe coring disturbance. CALA03 is entirely deformed, due to collapse of gas cracks during core storage. Low radiodensity contrast in the upper organic-rich part of lake Calafquén hindered detection of SSDS for the AD 1960 earthquake. For both lakes, potential deformation by the AD 2010 earthquake is not considered as uppermost sediment is highly susceptible to core disturbance by on-deck core handling and sealing, which hampers distinction between coring disturbance and SSDS.

4.2 Spatial Distribution of Sedimentary Imprint in Lakes Riñihue and Calafquén

Eight and nine cores of lake Riñihue contain a sedimentary imprint (i.e. centimeter-scale gaps or SSDS) linked to the AD 1960 and AD 1575 earthquake, respectively (Figure 8). For the AD 1837 earthquake, centimeter-scale gaps and SSDS occur predominantly on the northern slope. The AD 2010, AD 1737 and AD ~1466 earthquakes did not create detectable gaps at our core locations. For the AD 1737 earthquake, SSDS occur predominantly on the northern slope. For the AD ~1466 earthquake, one SSDS was identified on the northern slope.

In lake Calafquén, centimeter-scale gaps occur throughout the basin for AD 1960 and two centimeter-scale gaps—one in the western and one in the eastern basin—can be linked to the AD 1575 earthquake (Figure 9). For the AD 2010 earthquake, two gaps are located on the north-western slope. The AD 1837, AD 1737 and AD ~1466 earthquakes produced SSDS in both the western and eastern basin, but no gaps.

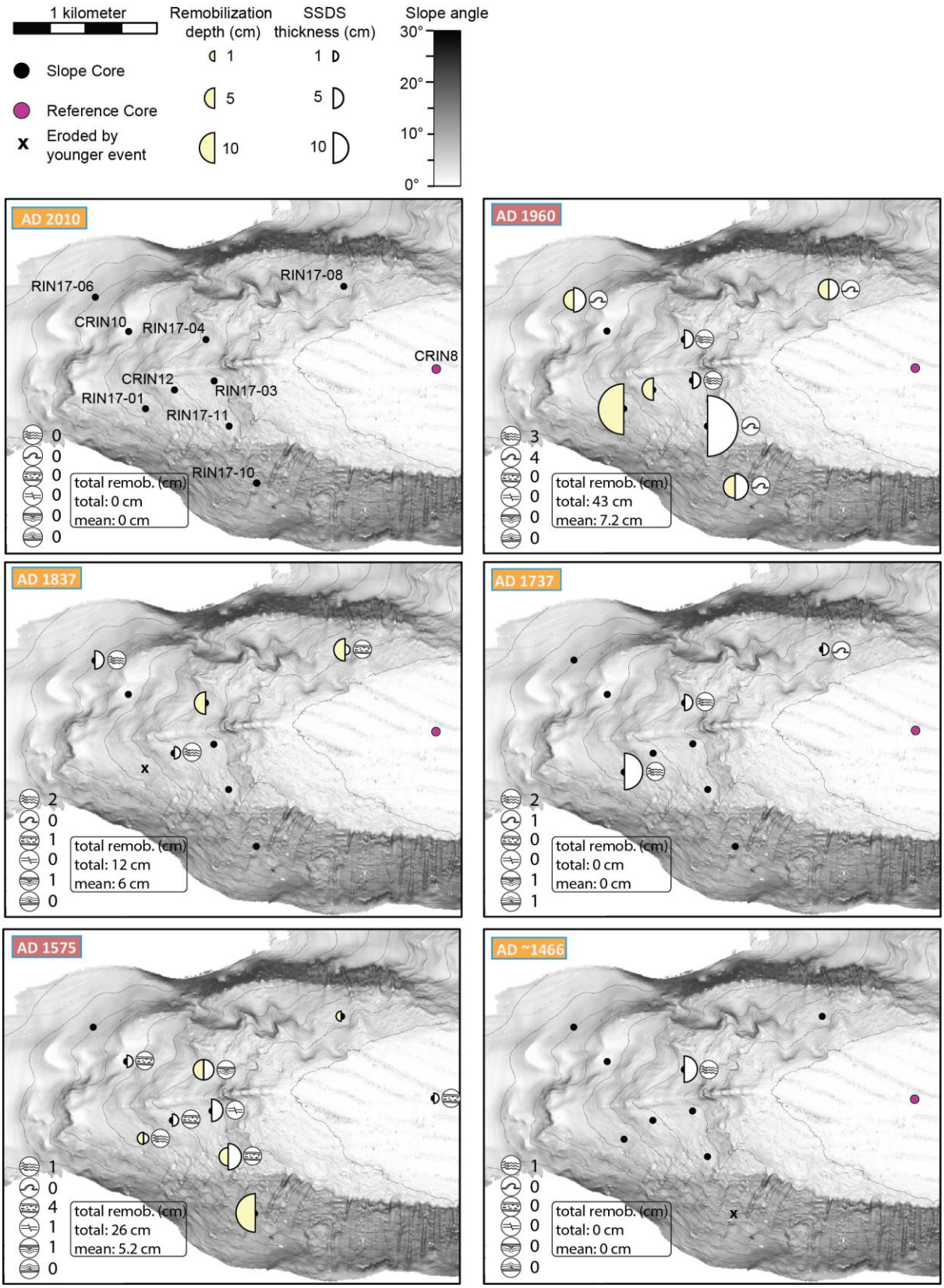

Figure 8 Spatial distribution and thickness of centimeter-scale gaps and SSDS for the six megathrust earthquakes recorded at lake Riñihue. SSDS type next to core site only depicts the strongest deformation observed for the corresponding earthquake. Below each map is a summary of all SSDS types and total remobilization depth.

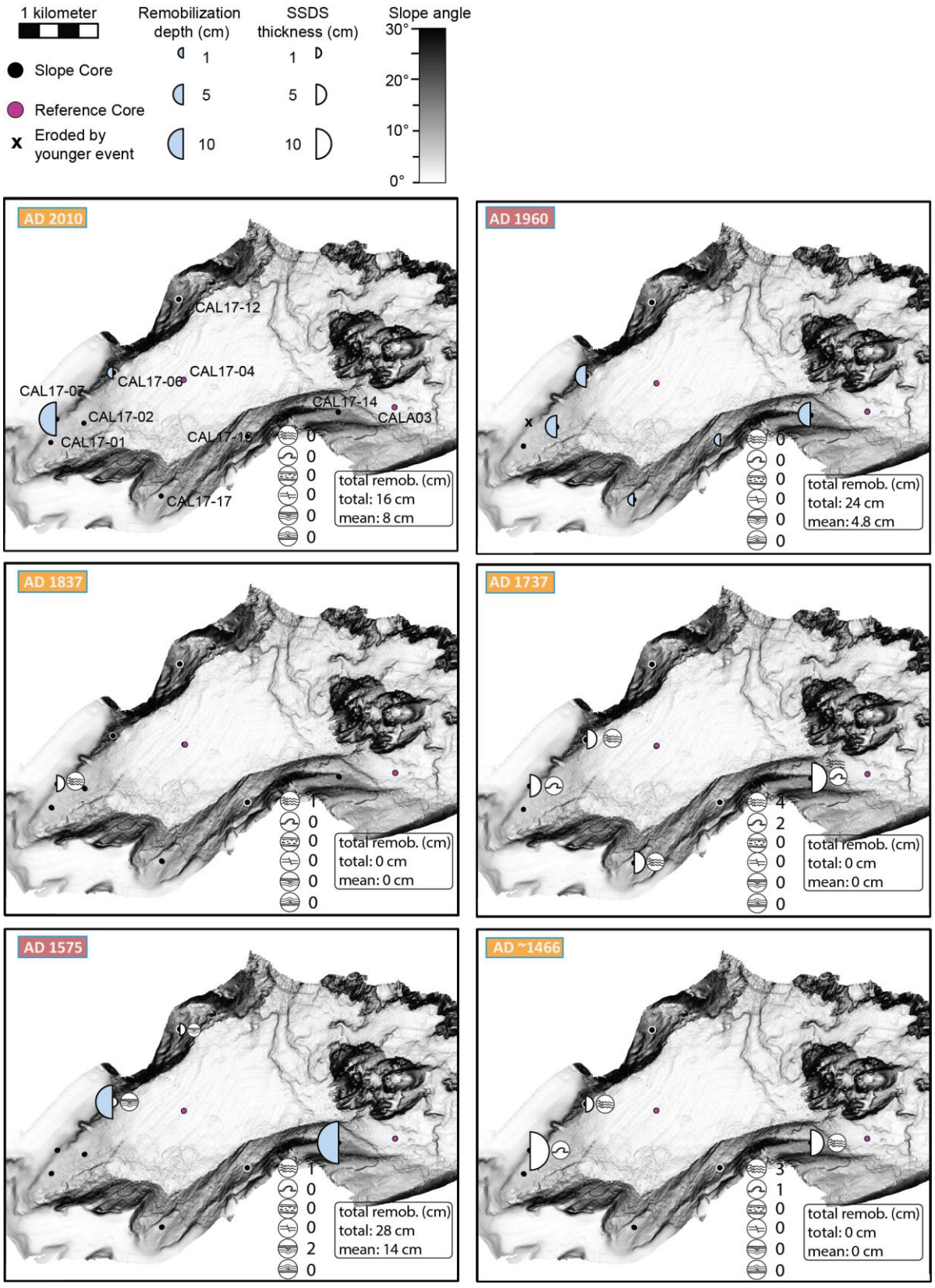

Figure 9 Spatial distribution and thickness of centimeter-scale gaps and SSDS for the six megathrust earthquakes recorded at lake Calafquén. SSDS type next to core site only depicts the strongest deformation observed for the corresponding earthquake. Below each map is a summary of all SSDS types and total remobilization depth.

4.3 Total Remobilization Depth and SSDS Thickness versus Slope Angle

Total remobilization depth and total SSDS thickness increase with slope angle in both lakes (Figure 10). Low (<0.05) p values and high (>0.5) R^2 values for all four correlations statistically support this relationship. The increase is stronger in lake Riñihue than in lake Calafquén for both remobilization depth and SSDS thickness. At the studied sites, centimeter-scale gaps are only present on slopes with slope angle ≥2.3°, whereas SSDS also occurs in the basin on slope angles as low as 0.2°.

The minimum and maximum deviation of the slope angle measured over 12, 20 and 50 m cross-sections from the ArcGIS-derived slope angle (see section 3.1) is represented by the error bars in Figure 10. A small deviation (i.e. small error bar) indicates that slope angle was rather constant (i.e. for lake Riñihue), whereas a larger deviation indicates that the slope is more convex or concave (i.e. lake Calafquén).

RIN17-10, CALA03 and CAL17-13 are treated as outliers in the total SSDS thickness plot and excluded from the linear regression. RIN17-10 is located between gullies and shows second highest remobilization depths (i.e. 20 cm in total). Possibly, these high remobilization depths lead to underestimation of total SSDS thickness as SSDS intervals have been eroded by gravity flows in nearby gullies or earthquake-triggered surficial remobilization. CALA03 is entirely disturbed by faults related to collapse of gas cracks during core storage. CAL17-13 has low radiodensity contrast in background sediment inhibiting the detection of disturbed lamination—the most common SSDS in lake Calafquén—leading to a likely underestimation of SSDS in this core.

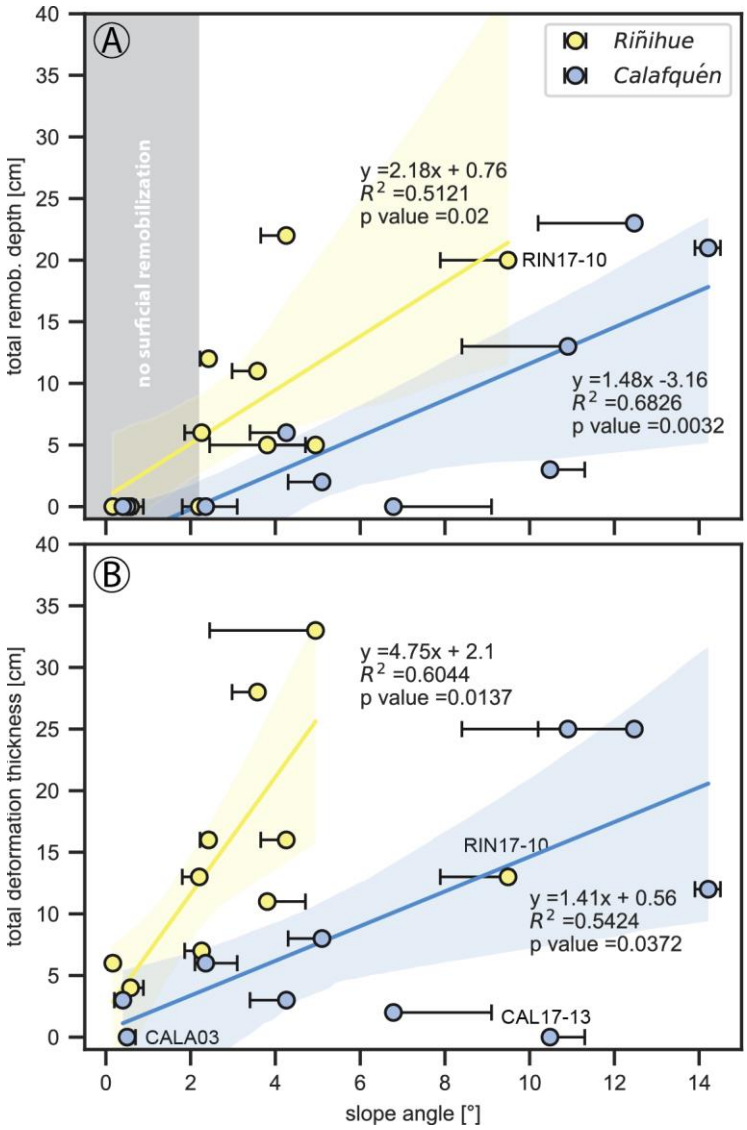

510

511 *Figure 10 Total remobilization depth and deformation thickness versus slope angle for all core sites*
512 *along with 95% bootstrap confidence intervals. Total deformation thickness includes both earthquake-correlated*
513 *and non-earthquake-correlated SSDS. Error bars display the maximum and minimum deviation of slope angles*
514 *measured over 12, 20 and 50 meters cross-sections from the ArcGIS-derived slope angle.*

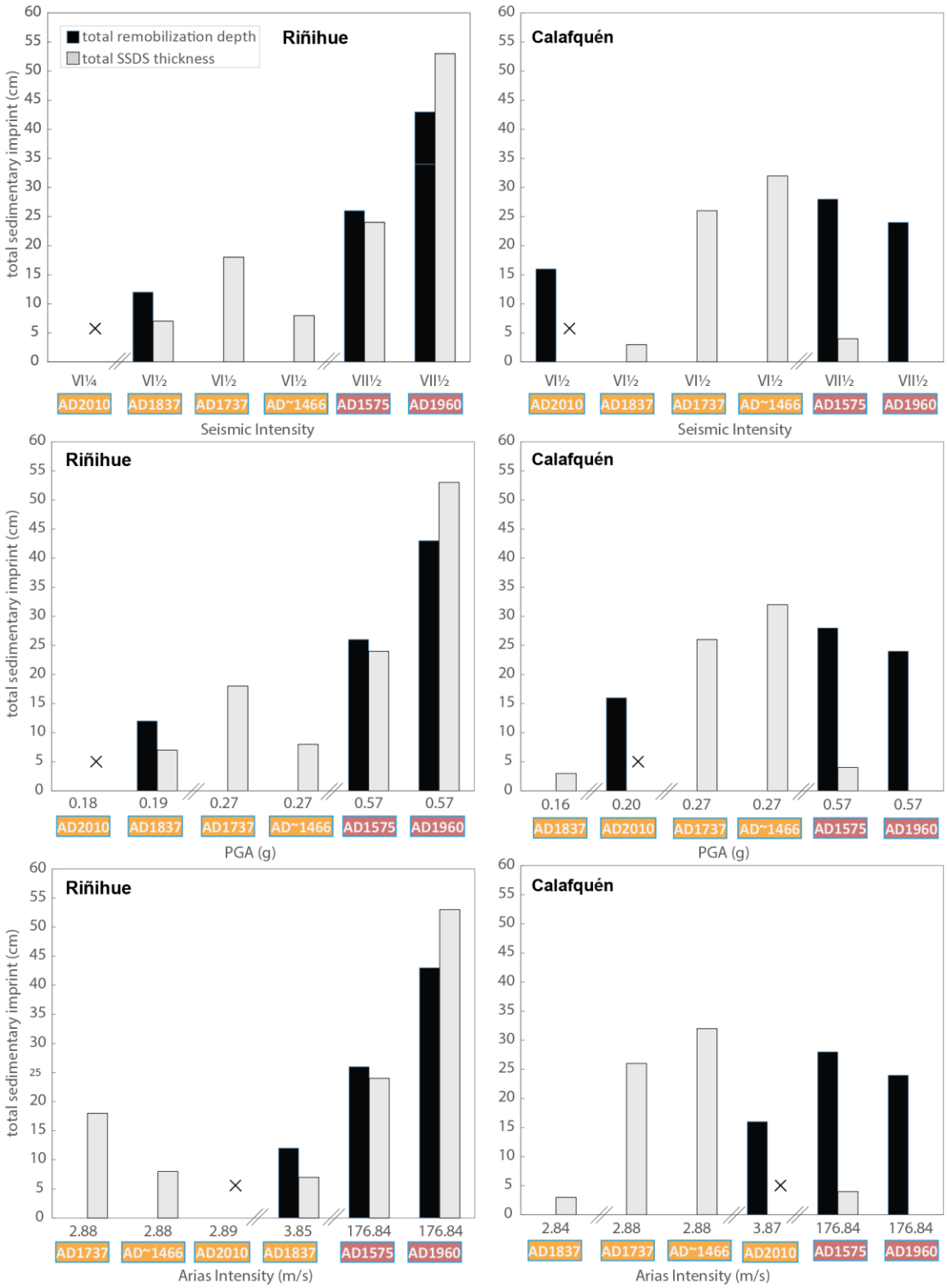

Figure 11 Total sedimentary imprint (cm) per lake represented by total remobilization depth and total SSDS thickness for each of the six megathrust earthquakes and depicted for seismic intensity, PGA and Ia.

4.4 Sedimentary Imprint Compared to Ground Motion Parameters

Total remobilization depth correlates best with I_a (Figure 11). Centimeter-scale gaps, with a total remobilization depth of 12 cm, occur from I_a 3.85 m/s caused by the M_w~9 AD 1837 earthquake in lake Riñihue (Table 2). The M_w 8.8 AD 2010 earthquake caused similar I_a of 3.87 m/s at lake Calafquén and a total remobilization depth of 16 cm. In both lakes, the M_w 9.5 AD 1960 and AD 1575 earthquakes generated highest total remobilization depth and highest I_a (176.84 m/s), PGA (0.57 g) and seismic intensity (VII$^1/_2$). The M_w ~7.7 AD 1737 and AD ~1466 earthquakes with I_a 2.88 at both lakes did not create gaps at our coring sites.

At the core sites of lake Riñihue, SSDS count and thickness correlate best with PGA (Figure 12). Most SSDS were produced during the AD 1960 and AD 1575 earthquakes with highest PGA (0.57 g). Folds are abundant for the AD 1960 earthquake and intraclast breccias for the AD 1575 earthquake, both with 4 occurrences. The M_w ~9 AD 1837 earthquake (PGA 0.19 g) and M_w~7.7 AD 1737 and AD ~1466 earthquakes (PGA 0.27 g) induced a lower SSDS count and thickness dominated by occurrence of disturbed laminations.

At the core sites of lake Calafquén, the AD 1737 and AD ~1466 earthquakes (PGA 0.27 g) caused highest SSDS counts and thickness. Also, the only three folds observed in this lake correspond to these earthquakes.

Table 2 Seismic intensity (Moernaut et al., 2014) and calculated ground motion parameters for each megathrust earthquake along with total remobilization depth and SSDS thickness. Deformation for the AD2010 earthquake was not considered as top most sediment is highly susceptible to coring disturbance.

	M_w	MMI		PGA (g)		I_a (m/s)		total remobilization depth (cm)		total EQ-related SSDS thickness (cm)	
Earthquake (AD)		Riñ	Cal	Riñ	Cal	Riñ	Cal	Riñ	Cal	Riñ	Cal
2010	8.8	VI$^1/_4$	VI$^1/_2$	0.18	0.20	2.89	3.87	0	16	-	-
1960	9.5	VII$^1/_2$	VII$^1/_2$	0.57	0.57	176.84	176.84	43	24	53	0
1837	9.0	VI$^1/_2$	VI$^1/_2$	0.19	0.16	3.85	2.84	12	0	7	3
1737	7.7	VI$^1/_2$	VI$^1/_2$	0.27	0.27	2.88	2.88	0	0	18	30
1575	9.5	VII$^1/_2$	VII$^1/_2$	0.57	0.57	176.84	176.84	26	28	24	3
~1466	7.7	VI$^1/_2$	VI$^1/_2$	0.27	0.27	2.88	2.88	0	0	8	25

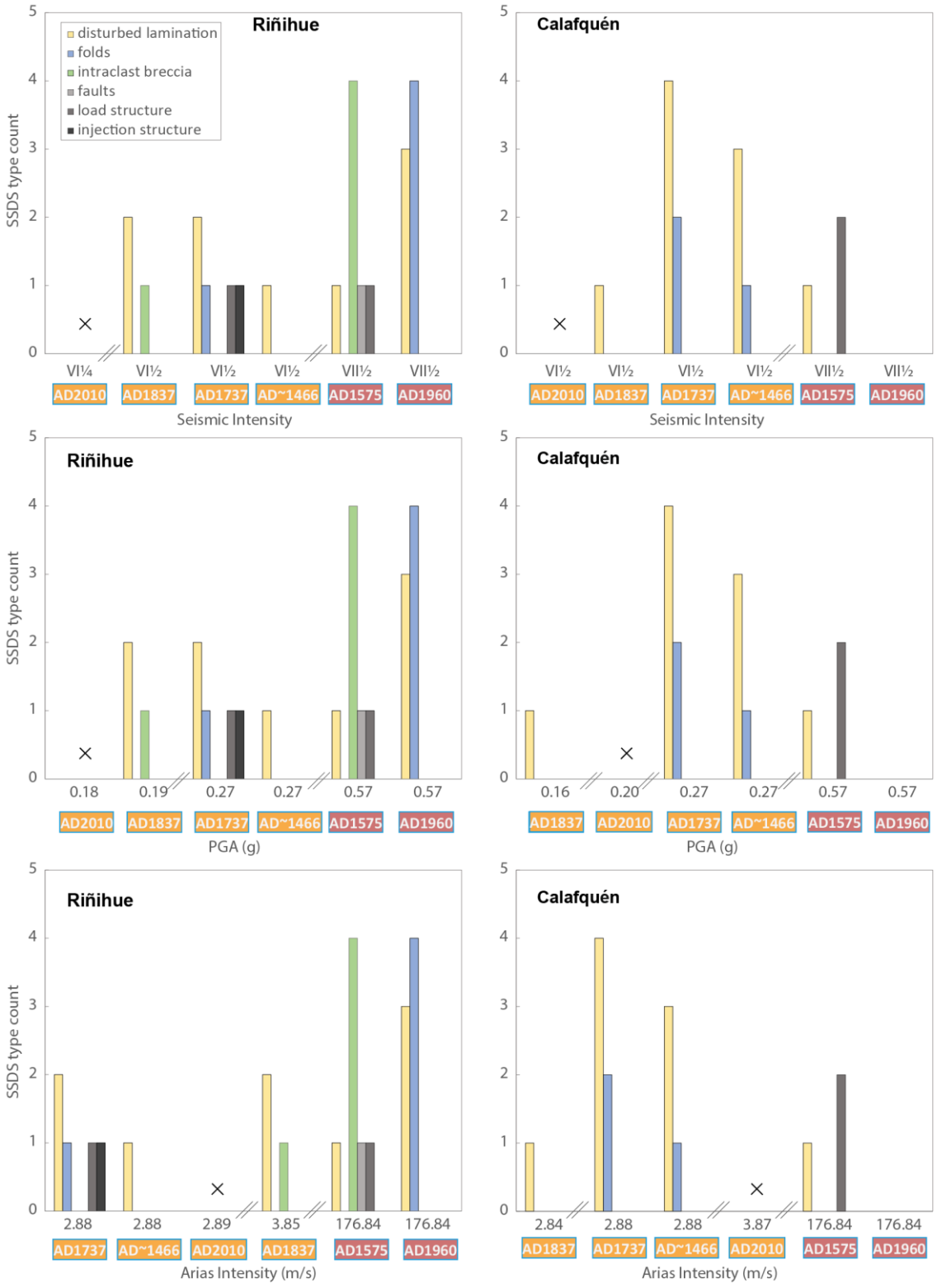

Figure 12 Count of SSDS types for each of the six megathrust earthquakes represented by total remobilization depth and total SSDS thickness depicted for seismic intensity, PGA and Ia.

Preprint manuscript: submitted to Sedimentology on 17.08.2020 (Molenaar et al.)

5 Discussion

5.1 Is It Possible to Track Centimer-Scale Gaps and SSDS Through Stratigraphic Correlation?

Our proposed method of stratigraphic correlation to well-dated seismo-turbidite records proved successful as centimeter-scale gaps and SSDS were detected in slope sequences and linked to six well-documented megathrust earthquakes. Using 3D medical CT scans, SSDS were identified that would have remained undetected in 2D by visual inspection of the split core surface or radiograph images (Figure 5c and Figure 6e).

The detection limit and precision of both centimeter-scale gaps and SSDS is strongly controlled by radiodensity and colour contrasts between background laminations and the presence of distinct marker layers of volcanic origin. The smallest identified remobilization gaps had thickness of ~1 cm and their detection was only possible because of distinct layers of low and high radiodensity directly below the stratigraphic level of this earthquake (AD 1575 earthquake, RIN17-08; Figure S8 in supporting information) or a clear unconformity at the top of a fold (AD 1960, RIN17-11; Figure 5e).

Overall, detection of gaps and identification of SSDS was easier for lake Riñihue due to higher proxy variation within the sediment. SSDS detection for lake Calafquén, especially for disturbed laminations, proved more complicated as there is less contrast in radiodensity between background laminations and frequent gas cracks disturb the lower part of some cores. Therefore, it is possible that some subtle SSDS in lake Calafquén were undetected leading to underestimation of SSDS.

Large differences between sedimentation rates between slope and basin would lead to decrease in accuracy when determining remobilization depths as this value is measured from the basin core sequence (methods section 3.4). Undeformed slope interval thicknesses above or below centimeter-scale gaps in the studied slope sequences are averagely 94% in lake Riñihue and 92% in lake Calafquén, suggesting similar sedimentation rates on the slope and in

566 the basin. At water depths of ≤79 m in lake Calafquén, the upper organic-rich section and lahar
567 deposits directly above and below the AD 1960 earthquake marker are less thick than in the
568 deeper basin, which would potentially lead to thickness underestimation of AD 1960-related
569 gaps. To correct for this, the thickness of AD 1960-related gaps at these depths are determined
570 by correlation to an intact slope core (i.e. CAL17-01) of similar water depth instead of the
571 reference basin sequence (Figure S9 and S10 in the supporting information).

572 We consider the remobilization depths derived from the reference basin core as
573 maximum values but of sufficient accuracy for our comparative analyses.

574 The detection of gaps and SSDS and their correlation to the six megathrust earthquakes
575 also depends on balance between sedimentation rate and earthquake recurrence as earthquake
576 impact can "overprint" gaps or SSDS created by older earthquakes (Agnon et al., 2006;
577 Molenaar et al., 2019). This could lead to overestimation of remobilization depth for the
578 younger and underestimation for the older earthquake as gaps are entirely associated to the
579 youngest event (Figure 4a and section 3.6). In contrast, overprinting of SSDS could lead to
580 underestimation of SSDS thickness for the younger earthquake and overestimation for the older
581 one as we split and assign a disturbed lamination interval correlating to two earthquakes to both
582 earthquakes (Figure 4e). High sedimentation rates and long earthquake recurrence intervals
583 enhance the reliability of sedimentary imprint to earthquake assignment as younger
584 earthquakes are less likely to overprint the evidence of older earthquakes.

585 ## 5.2 Did Mechanisms Other than Seismic Shaking Create Centimeter-Scale Gaps or SSDS?

586 ### 5.2.1 Are all Centimeter-Scale Gaps Related to one of the Six Megathrust Earthquakes?

587 Aside from seismic shaking, centimeter-scale erosional gaps in lacustrine sediment
588 sequences may be caused by wave action, lake level fluctuations, seiches or hyperpycnal flows.
589 The minimum water depth of our study sites is 39 m (RIN17-06) making shallow-water
590 mechanisms irrelevant and ruling out wave action and small lake level fluctuation as potential

591 causes of erosion or deformation. Large lake level fluctuations (> 5 m) have not occurred in
592 these open lake systems located in a temperate rainy climate. Erosion by seismic seiches is
593 dismissed as the erosional impact of seiches would decrease with water depth (Wiegel, 1964)
594 and remobilization thickness does not correlate with water depth. Also, no seiches were
595 reported for the AD 2010 and AD 1960 earthquakes at both lake basins (Van Daele et al.,
596 2015). Study sites are located away from any major river or lahar inflow (Figures S1 and S2 in
597 the supporting information), thus excluding erosion by any river-related or lahar-induced
598 hyperpycnal flows.

599 All centimeter-scale gaps correlate to the six megathrust earthquakes suggesting
600 seismic shaking as the dominant trigger for surficial erosion at our studied slope sites. Of the
601 12 thin (i.e. ~1 cm) earthquake-related turbidites observed in the slope cores of lakes Riñihue
602 and Calafquén, only 6 are located above a centimeter-scale gap in the sequence. Also, some
603 turbidites with a sandy—and potentially more erosive—base are actually not located above a
604 gap. Therefore, we propose that erosion related to thin turbidites on the slope is negligible as
605 erosion would otherwise be consistently observed below these deposits. This is supported by
606 intralake basin core correlation as basin lacustrine turbidites caused no observable erosion and
607 age-depth models were continuous (Van Daele et al., 2014; Moernaut et al., 2014).

608 Two sites in lake Riñihue do show the potential of significant additional erosion by
609 erosive downslope flows: RIN17-10 is located in the southern gully system and RIN17-01
610 includes an AD 1960-related event deposit with lamination fragments whose causative gravity
611 flow was potentially erosive (Figure 1 and Figure S1 in the supporting information). Gaps at
612 both locations correspond to highest observed remobilization depths with 20 cm (AD 1960,
613 RIN17-01) and 14 cm (AD 1575, RIN17-10).

We relate all observed cm-scale gaps to earthquake-triggered surficial remobilization, while emphasizing the importance of selecting coring locations sheltered from any gully systems and deep enough to exclude shallow-water erosive processes.

5.2.2 Are all SSDS Related to one of the Six Megathrust Earthquakes?

Earthquakes, but also non-seismic processes, such as rapid sediment loading and groundwater flow can trigger deformation of near-surface sediments (Owen and Moretti, 2011). Wave action is a potential cause of deformation, but can be excluded due to sufficient water depth of our coring locations (see section 2.2). Rapid sediment loading by turbidites or high-density tephra fall is an unlikely mechanism as load structures are not systematically present below such instantaneous deposits: only four load structures occur below tephra deposits and non below turbidites. Also, groundwater movement is ruled out as no pockmarks (i.e. seepage craters) can be observed on the bathymetric data near the study sites. Therefore, we propose seismic shaking as the main trigger of SSDS formation at the coring sites in lakes Calafquén and Riñihue.

Most SSDS intervals—65% and 56% in lake Riñihue and lake Calafquén, respectively—were confidently attributed to one of the six strong megathrust earthquakes. We suggest that SSDS intervals which are not within 2 cm of the six earthquake markers were either caused by i) an unknown local prehistorical earthquake or ii) one of the six megathrust earthquakes but were induced by dewatering of a deeper tephra or lahar deposit, weakening the overlying sediment and facilitating deformation, a mechanism outlined in Moernaut et al. (2019). This latter mechanism may be particularly relevant for our study sites as 13 from 19 SSDS intervals that are not correlated to the six megathrust earthquakes are located above a tephra or lahar deposit. For example, in lake Riñihue, 5 out of 10 cores (RIN17-01, CRIN12, CRIN10, RIN17-08 and RIN17-10) include SSDS intervals directly overlying the bright lahar

638 deposit 8 cm below the stratigraphic level of the AD~1466 earthquake. Dewatering of the lahar
639 deposit during the AD~1466 earthquake could have created these SSDS.

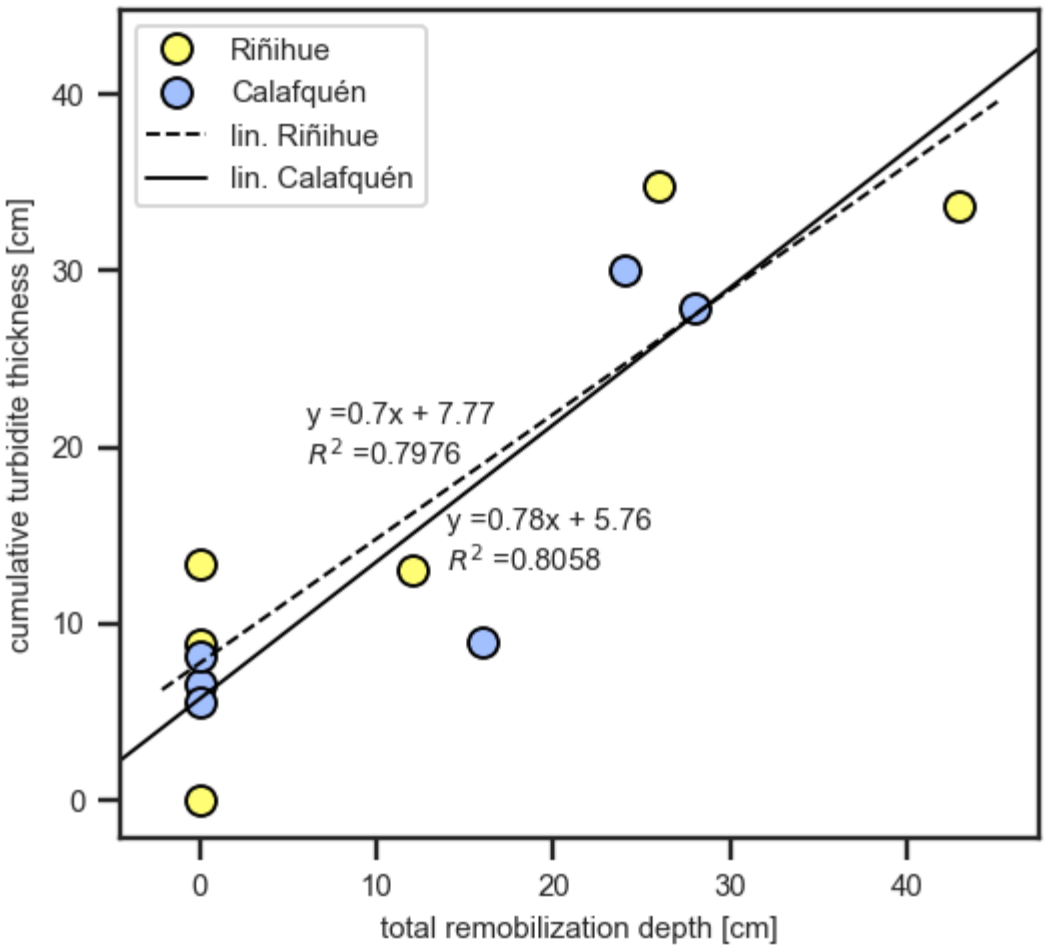

640

641 *Figure 13 Cumulative turbidite thickness per lake—summing up turbidite thicknesses determined by*
642 *Moernaut et al. (2014) and thicknesses in our reference basin cores—versus total remobilization depth (this study)*
643 *for each of the six megathrust earthquakes.*

644 ## 5.3 How Does Surficial Remobilization in the Studied Lakes Compare to Observations at other
645 Settings?

646 ### 5.3.1 Does Surficial Remobilization Occur Uniformly over Extensive Slope Areas?

647 Previous research suggested surficial remobilization to occur uniformly over large
648 slope segments as near-surface sediments are likely to have similar geotechnical characteristics
649 (Ashi et al., 2014; Moernaut et al., 2017). However, our detailed slope mapping reveals that
650 surficial remobilization occurs in a patchier way as the occurrence and thickness of

remobilization along the slopes of the studied basins varies strongly (Figure 8 and Figure 9). We suggest that sedimentary imprint during seismic shaking is modulated by site-specific characteristics including i) local seismic site effects; ii) geotechnical characteristics of the near-surface sediments and iii) local slope morphology.

Seismic site effects include amplification and frequency content moderation or filtering and is controlled by sediment to bedrock thickness, irregularities in the bedrock morphology (e.g. ridges or islands) and topography (e.g. Kawase, 2003). Geotechnical characteristics such as shear strength, friction or cohesion of near-surface sediments control their erodibility (e.g. Grabowski et al., 2011). Previous earthquakes might alter geotechnical characteristics as seismic shaking can compact near-surface sediment, thereby increasing sediment shear strength (i.e. seismic strengthening; e.g. Sawyer and DeVore (2015), Molenaar et al. (2019)). Morphological factors include slope angle and slope orientation, as gravitational shear stress increases with slope angle and slopes facing away from the seismic source can experience amplified shaking (Meunier et al. (2008); see section 5.5.2 for more detailed discussion).

5.3.2 How Significant is Surficial Remobilization as an Earthquake-Triggered Remobilization Process?

Moernaut et al. (2017) proposed earthquake-triggered surficial remobilization as the main process behind turbidite records in the studied Chilean lake basins. The remobilization depths inferred from comparison of seismo-turbidite composition to that of surficial sediments (0.6-20.5 cm, average of ~5 cm) are very similar to remobilization depths derived by stratigraphic correlation of slope to basin cores in this study (1-20 cm, average of 6.7 cm). Moreover, for each event and lake, the cumulative turbidite thickness (Moernaut et al., 2014) correlates well with the total remobilization depth determined in this study (Figure 13). The AD 1737 and AD ~1466 earthquakes in both lakes and the AD 1837 in lake Calafquén did trigger turbidity currents which created small turbidites within the basin, but did not cause

676 detectable gaps within our studied slope sequences. Possibly, erosion occurred at steeper
677 slopes, which are more susceptibble to erosion, but were not cored during this study. We
678 confirm the hypothesis that surficial remobilization is the main remobilization process creating
679 the seismo-turbidites in the studied basins and not, as commonly assumed, earthquake-induced
680 slope failures and subaqueous landslides. This finding is highly significant for assessing the
681 reliability of long turbidite paleoseismic records (Moernaut et al., 2017) as surficial
682 remobilization can facilitate continuous seismo-turbidite records despite a lack of landslide
683 scars.

684 At the Japan Trench, surficial remobilization during the M_w 9.0 AD 2011 Tohoku-oki
685 earthquake eroded and transported sufficient surficial sediment to create widespread seismo-
686 turbidites with elevated $xs^{210}Pb$ activities at 100's of kilometers along the Japan Trench
687 (McHugh et al., 2016; McHugh et al., 2020) and to move vast amounts of organic carbon into
688 the trench (Kioka et al., 2019). Recent studies on radiocarbon composition of seismo-turbidites
689 showed that surficial remobilization was also a relevant remobilization process during past
690 Japan Trench megathrust earthquakes (Schwestermann et al., 2020; Ikehara et al., 2020).
691 Furthermore, Molenaar et al. (2019) detected gaps with remobilization depths comparable to
692 this study (i.e. 4-12 cm) directly on a Japan Trench slope (3138 m water depth) and correlated
693 these to the largest historical earthquakes in the region including the AD 2011 Tohoku-oki
694 earthquake.

695 Based on these observations of widespread surficial remobilization at both settings, we
696 propose that surficial remobilization is a common remobilization process during strong seismic
697 shaking in both lakes and ocean, capable of transporting vast amounts of sediment into terminal
698 basins.

5.4 What are the Driving Mechanisms for Deformation in Lake Riñihue and Lake Calafquén?

Disturbed laminations, folds and intraclast breccias are the most common SSDS in lakes Riñihue and Calafquén and mainly occur in background sediment (Figure 12). Inverse density gradients can induce Rayleigh-Taylor instabilities and are a common driver of SSDS formation (Owen, 2003). Background sediment in both lakes does not show large density variation (Figure S12 in the supporting information); therefore, we rule out Rayleigh-Taylor instability as the dominant driving mechanism for these SSDS. Similar types of SSDS are observed in the stable stratified sediment (i.e. density increasing with depth) of the Lake Lisan Formation along the Dead Sea (Marco and Agnon, 1995) and were linked to Kelvin-Helmholtz Instability (KHI) (Heifetz et al., 2005). KHI involves deformation through shear stress build-up along the interface of stable stratified sediment layers due to the velocity difference of these layers during seismic shaking caused by minor variation in density and viscosity within background sediment. We propose KHI as the dominant driving mechanism of disturbed lamination, folds and intraclast breccia in our studied lakes.

Other SSDS that sporadically occur at our study sites are, listed from most common to less common, load structures, faults and injection structures. Load structures only formed in high-density material like tephra and lahar deposits that are present as intercalations in the background sediment. Therefore, we explain these structures with the aforementioned Rayleigh-Taylor instability process controlled by inverse density gradients. Faults are rare in our studied lakes with two occurrences in RIN17-03, related to the AD 1575 earthquake, and CRIN8, not stratigraphically linked to one of the six megathrust earthquakes. Faults form if strain rates during seismic shaking exceed the yield strength of elastically-behaving sediment (Owen, 1987) and have been reported and linked to earthquakes in different lithologies and settings (e.g. Becker et al., 2002; Monecke et al., 2004; Rodríguez-Pascua et al., 2010). The only injection structure developed above a tephra layer in core RIN17-01 (lake Riñihue) below

724 an AD 1960-related event deposit. Injection structures occur when a sediment becomes
725 fluidized as pore pressure exceeds the overburden stress and tensile strength of the capping
726 layer. Sudden loading by the overlying event deposit may have enhanced pore pressure and
727 simultaneously acted as a lower-permeability layer, thereby increasing pore pressure while
728 inhibiting immediate pore pressure dissipation.

729 Load and injection structures are driven by Rayleigh-Taylor instabilities and
730 fluidization processes, respectively (Owen, 2003), and are—in first order—controlled by
731 availability of density contrasts and liquefaction potential of available sediment. This explains
732 the scarcity of such structures in the dominantly fine-grained varved background sediment
733 intercalated with relatively thin and irregularly spaced volcanic layers. Also, load and injection
734 structures do not necessarily occur at the sediment-water interface (Rodríguez-Pascua et al.,
735 2000), hampering correlation to specific earthquakes and reducing their paleoseismological
736 value in our study sites.

737 ## 5.5 How Does Morphology Modulate Surficial Remobilization and Deformation?

738 ### 5.5.1 What is the Effect of Slope Angle?

739 Both remobilization depth and SSDS thickness increase with slope angle at the studied
740 slope sites of lakes Riñihue and Calafquén (Figure 10), suggesting gravity as a key driving
741 mechanism for surficial remobilization and deformation. Gravitational downslope stress
742 increases with slope angle, thereby enabling downslope movement of remobilized and
743 plastically-deforming sediment. Increased surficial remobilization at higher slope angles—
744 higher than the maximum 9.5° for lake Riñihue and 14.2° for lake Calafquén—might cause
745 significant erosion of SSDS intervals, potentially leading to underestimation of SSDS thickness
746 at these slope angles.

747 Surficial remobilization only occurs from a ≥2.3° slope angle, which seems to provide
748 the minimum required gravitational stress at our study sites to enable sediment remobilization

749 and downslope transportation. In contrast, SSDS are present in the nearly-flat basin at slope
750 angles of only 0.2° suggesting that seismically-induced shear stress alone can suffice to deform
751 sediment. Previous research on folded layers within the Lake Lisan Formation reported SSDS
752 at slope angles of <1° and related vergence of folds to the paleo slope direction (Alsop and
753 Marco, 2012, 2013), which demonstrates the high sensitivity of SSDS development to small
754 variations in gravitational downslope stress.

755 For lake Calafquén, remobilization depth and SSDS thickness increase less with slope
756 angle than for lake Riñihue. This could be due to a higher diatom content in the background
757 sediments of lake Calafquén illustrated by a combination of lower magnetic susceptibility and
758 abundant bright green laminations identified as diatom blooms (Moernaut et al., (2014); Van
759 Daele et al., (2015)). Through high particle interlocking and surface roughness, sediments'
760 shear strength increases with diatom content (Wiemer and Kopf, 2017) resulting in lower
761 erodibility and lower susceptibility to shear-induced deformation.

762 ### 5.5.2 What is the Effect of Slope Facing?

763 Slope facing can modulate the seismically-induced sedimentary imprint as oblique
764 incoming seismic waves can be amplified on slopes facing away from the seismic source, a
765 process supported by numerical modelling and locally-enhanced earthquake-induced landslide
766 occurrence (Meunier et al., 2008). Following this hypothesis, we may expect enhanced
767 sedimentary imprint—centimeter-scale gaps and more-developed SSDS like folds and
768 intraclast breccia (see section 5.4)—on i) south facing slopes for the northern AD 2010
769 earthquakes, ii) on north facing slopes for the southern AD1837 earthquake and iii) on all slope
770 facings for the AD 1960, AD 1575, AD 1737 and AD ~1466 earthquakes, the rupture areas of
771 which extend north and south of our studied basins (Figure 1).

772 Widespread sedimentary imprint occurs on all slope orientations for the strongest M_w
773 ~9.5 AD 1960 and AD 1575 earthquakes (Figure 8 and Figure 9). Folds are scarce for AD 1737

774 earthquake but occur on different slope facings: a south-east and north facing slope in lake
775 Calafquén and another south-east facing slope in lake Riñihue. The AD ~1466 earthquake
776 created one fold on a south-east facing slope in lake Calafquén. The northern AD 2010
777 earthquake induced two centimeter-scale gaps both on a south-east facing slope in lake
778 Calafquén. All these observations correspond well with our hypothesis. The only exception is
779 the southern AD 1837 earthquake which induced a centimeter-scale gap on an east facing slope
780 and another centimeter-scale gap along with an intraclast breccia on a south-east facing slope,
781 whereas our hypothesis predicts the main impact would be on north-facing slopes. Possibly,
782 other factors, such as local seismic site effects, geotechnical characteristics (see section 5.3.1)
783 or slope angle, had a stronger control on sediment remobilization and deformation than
784 amplification facilitated by slope facing.

785 We suggest that our data is inconclusive regarding the amplification of seismic waves
786 on slopes facing away from the seismic source. The influence of other factors seems to overrule
787 this effect and result in sedimentary imprint on other slope facings.

788 ## 5.6 Which Ground Motion Characteristics Control Surficial Remobilization and Deformation?

789 ### 5.6.1 Surficial Remobilization Controlled by Long Duration and Low Frequency Content

790 The occurrence and thickness of surficial remobilization at the studied slope sites in
791 lakes Riñihue and Calafquén correlates best with I_a as centimeter-scale gaps occur from an I_a
792 of 3.85 m/s (Figure 11). Arias intensity uses the time integral of the squared acceleration and
793 depends on several ground motion characteristics (i.e., duration, amplitude, frequency content).

794 Additionally, the M_w 8.8 AD 2010 earthquake is the lowest magnitude megathrust
795 earthquake which created observable gaps at the studied sites in lake Calafquén suggesting
796 that—aside from sufficient shaking intensity (i.e. I_a)—a minimum magnitude is required to
797 enable surficial remobilization at these sites. Remobilization must have also occurred for the
798 lower magnitude (M_w ~7.7) AD 1737 and AD ~1466 earthquakes as these earthquakes link to

small turbidites within the studied basins (Moernaut et al., 2014). Possibly, surficial remobilization for the AD 1737 and AD ~1466 earthquakes occurred on steeper slopes, which are more susceptible to remobilization (section 5.5.1), but not cored during our field campaign.

Molenaar et al. (2019) proposed a magnitude threshold of M_w 8 for surficial remobilization at a Japan Trench slope site. Only earthquakes of M_w >8 caused detectable centimeter-scale gaps at the specific site, despite regional M_w <8 earthquakes having PGA values similar or even higher than the M_w >8 earthquakes (~0.6 g). Therefore, Molenaar et al. (2019) suggested that surficial remobilization relies more on shaking duration or frequency content than amplitude (i.e. PGA) as higher magnitude earthquakes generally correspond to longer duration (Meier et al., 2017) and more low frequency content.

The AD 1837 and AD 2010 ruptures did cause surficial remobilization in lake Riñihue and lake Calafquén, respectively, despite their large distance to the lakes of 210 km and 170 km. As especially the high-frequency ground motion content attenuates with distance, longer travel distances would result in ground motion dominated by low frequency components (e.g. Anderson and Hough, 1984). This is in line with observations for the M_w 9.0 AD 2011 Tohoku-oki earthquake: turbidites triggered by remobilization of surficial slope sediment were identified as far as ~100 km from the area of maximum slip (McHugh et al., 2016). Recently, McHugh et al. (2020) linked the widespread distribution of AD 2011 turbidites to long-period seismic waves, which would not only attenuate less than short-period waves, but also resonate in the Japan wedge, thereby amplifying and extending the duration of low frequency ground motion.

In line with recent studies, we suggest that long duration and low frequency content of ground motion favors surficial remobilization. Dedicated experiments are required to investigate how exactly these factors interact with surficial sediments.

5.6.2 SSDS Controlled by Amplitude of Ground Acceleration

For lake Riñihue, occurrence and type of SSDS correlate best with PGA (Figure 12). The AD 1960 and AD 1575 earthquakes correspond to highest PGA as well as highest count of more developed SSDS (i.e. folds and intraclast breccias). The AD 1737 and AD 1837 earthquake only caused one detected fold and one intraclast breccia in lake Riñihue, respectively. Previous research at the Lake Lisan Formation showed that KHI-related SSDS develop from disturbed lamination to folds and finally intraclast breccia with increasing PGA (Heifetz et al., 2005; Wetzler et al., 2010). Numerical models predict that disturbed lamination occurs from ~0.1-0.15 g, folds from ~0.2-0.25 g and intraclast breccia from ~0.5-0.6 g at layer thicknesses of <10 cm (Wetzler et al., 2010). Despite very different lithology, our observations in Chile correspond very well with these PGA values and related SSDS types as we observe disturbed lamination from ~0.18 g due to the AD 1837 earthquake, a fold from ~0.27 g related to the AD 1737 earthquake and abundant intraclast breccias from ~0.57 g induced by the AD 1575 earthquake. The only exception is a single intraclast breccia observed for the AD 1837 earthquake in lake Riñihue. Based on an unprecedented comparison of SSDS in sediment cores and ground motion parameters of historical earthquakes, we confirm that the amplitude of ground accelerations is the main seismological control on the occurrence and development of KHI-related SSDS.

For lake Calafquén, the AD 1737 and AD ~1466 earthquakes, which had similar magnitudes (M_w ~7.7) and rupture location, caused similar SSDS imprint. These are the only earthquakes in lake Calafquén that produced detectable folds. No clear correlation exists between KHI-related SSDS development and PGA in lake Calafquén. Possible explanations are that i) SSDS for the AD 1960 and AD 1575 earthquakes were underestimated due to lack in radiodensity contrast and abundant gas cracks (section 5.1); ii) SSDS for the AD 1960 earthquake were eroded by surficial remobilization as 5 out of 7 slope cores contain AD 1960-

related centimeter-scale gaps or iii) KHI-related deformation, which requires stable stratified sediment (i.e. density increasing with depth), was hampered during the AD 1575 earthquake by a high-density tephra a few mm below the AD 1575 stratigraphic level (Figure 6).

6 Conclusion

Our study directly links sedimentary imprint (i.e. centimeter-scale gaps and SSDS) on 17 slope sites in two Chilean lakes with the ground motion parameters of six well-documented megathrust earthquakes. We present the following conclusions:

1. Surficial remobilization and deformation of slope sediments can be detected and linked to seismo-turbidite records using detailed stratigraphic correlation of slope sediment cores to well-dated basin sequences.
2. We identify seismic shaking as the cause of surficial remobilization and deformation by correlation to strong historical earthquakes and exclude other possible trigger mechanisms.
3. Most of the SSDS occurrences (i.e. 65% and 56% in lake Riñihue and lake Calafquén, respectively) stratigraphically link to one of the six studied megathrust earthquakes. Other SSDS occurrences might be related to i) other—possibly local—earthquakes or ii) the 6 megathrust earthquakes but deformation takes place somewhat deeper in the sequence due to dynamic response of both coarse- or fine-grained intercalated volcanic deposits (i.e. tephras or lahar deposits) during seismic shaking.
4. Surficial remobilization does not occur uniformly over large slope areas as it can be modulated by seismic site effects, local geotechnical characteristics (i.e. effect of older earthquakes) and morphological characteristics (i.e. slope angle and slope facing).
5. Surficial remobilization by strong seismic shaking is the main process of seismo-turbidite formation in our studied basins, which is in agreement with what has been inferred for the Japan Trench. This demonstrates that surficial remobilization is a

873 significant remobilization process capable of transporting vast amounts of sediments
874 into terminal basins of both lakes and ocean.
875 6. Steeper slope angle increases a slopes' susceptibility to earthquake impact due to
876 higher gravitational downslope stress. Surficial remobilization requires a minimum
877 slope angle (i.e. ≥2.3° at our study sites), whereas small-scale deformation is observed
878 at nearly flat basin sites of <1°.
879 7. The amount of surficial remobilization correlates best with Arias Intensity. Based on
880 our observations, we propose that surficial remobilization is enhanced by low
881 frequency content and long duration of ground motion.
882 8. Our study provides the first field-based data linking progressive development of KHI-
883 related SSDS (i.e. disturbed lamination to folds and intraclast breccia) with higher
884 PGAs. As deformation correlates best with PGA, we propose that surficial
885 deformation is most related to the amplitude of ground acceleration and not to its
886 duration.

887 **7 Acknowledgements**

888 The contribution of A. Molenaar and J. Moernaut is funded via the Austrian Science
889 Fund (FWF): project P30285-N34 and the Nachwuchsförderung 2016 of the University of
890 Innsbruck. We thank Wolfgang Recheis and Markus Erhardt from the Medical University
891 Innsbruck for acquisition of the medical CT data, as well as Rik Achten from the Ghent
892 University Hospital for access to the medical CT scanner. Maarten Van Daele thanks Research
893 Foundation – Flanders (FWO; project 1523315N and 12D6817N). Roberto Urrutia thanks the
894 ANID/FONDAP/15130015 project. For logistical and technical support during Chilean
895 fieldwork, we thank the Flanders Marine Institute (VLIZ), Robert Brümmer, Koen De Rycker,
896 Alejandro Peña and Daniel Martínez Olguín. Data is available from the authors upon
897 reasonable request.

8 References

Agnon, A., Migowski, C. and **Marco, S.** (2006) Intraclast breccias in laminated sequences reviewed: Recorders of paleo-earthquakes. *SPECIAL PAPERS-GEOLOGICAL SOCIETY OF AMERICA*, **401**, 195.

Allen, J.R., ed. (1982), *Sedimentary structures*, Elsevier, Amsterdam, 633 pp.

Alsop, G.I. and **Marco, S.** (2012) A large-scale radial pattern of seismogenic slumping towards the Dead Sea Basin. *Journal of the Geological Society*, **169**, 99–110.

Alsop, G.I. and **Marco, S.** (2013) Seismogenic slump folds formed by gravity-driven tectonics down a negligible subaqueous slope. *Tectonophysics*, **605**, 48–69.

Ambraseys, N.N., SIMPSON, K.A. and **BOMMER, J.J.** (1996) Prediction of horizontal response spectra in Europe. *Earthquake Engng. Struct. Dyn.*, **25**, 371–400.

Anderson, J.G. and **Hough, S.E.** (1984) A model for the shape of the Fourier amplitude spectrum of acceleration at high frequencies. *Bulletin of the Seismological Society of America*, **74**, 1969–1993.

Ashi, J., Sawada, R., Omura, A. and **Ikehara, K.** (2014) Accumulation of an earthquake-induced extremely turbid layer in a terminal basin of the Nankai accretionary prism. *Earth Planet Space*, **66**, 51.

Avşar, U., Jónsson, S., Avşar, Ö. and **Schmidt, S.** (2016) Earthquake-induced soft-sediment deformations and seismically amplified erosion rates recorded in varved sediments of Köyceğiz Lake (SW Turkey). *J. Geophys. Res. Solid Earth*, **121**, 4767–4779.

Becker, A., Davenport, C.A. and **Giardini, D.** (2002) Palaeoseismicity studies on end-Pleistocene and Holocene lake deposits around Basle, Switzerland. *Geophysical Journal International*, **149**, 659–678.

Bouma, A.H. (1962) Sedimentology of some flysch deposits. *Agraphic approach to facies interpretation*, **168**.

Campos, H. (1984) Limnological study of Araucanian lakes (Chile) With 1 figure and 3 tables in the text. *Internationale Vereinigung für theoretische und angewandte Limnologie: Verhandlungen*, **22**, 1319–1327.

Campos, H., Hamilton, D.P., Villalobos, L., Imberger, J. and **Javam, A.** (2001) A modelling assessment of potential for eutrophication of Lake Riñihue, Chile. *Archiv für Hydrobiologie*, 101–125.

Céspedes, S., Boroschek, R. and **Ruiz, R.** (2019) Modelos de movimiento fuerte para duración e Intensidad de Arias para registros de movimiento fuerte en Chile. *Conference: XII Congreso Chileno de Sismología e Ingeniería Antisísmica*.

Cifuentes, I.L. (1989) The 1960 Chilean earthquakes. *J. Geophys. Res.*, **94**, 665.

Cisternas, M., Atwater, B.F., Torrejón, F., Sawai, Y., Machuca, G., Lagos, M., Eipert, A., Youlton, C., Salgado, I., Kamataki, T., Shishikura, M., Rajendran, C.P., Malik, J.K., Rizal, Y. and **Husni, M.** (2005) Predecessors of the giant 1960 Chile earthquake. *Nature*, **437**, 404.

Cisternas, M., Carvajal, M., Wesson, R., Ely, L.L. and **Gorigoitia, N.** (2017) Exploring the Historical Earthquakes Preceding the Giant 1960 Chile Earthquake in a Time-Dependent Seismogenic Zone. *Bulletin of the Seismological Society of America*, **107**, 2664–2675.

DeMets, C., Gordon, R.G. and **Argus, D.F.** (2010) Geologically current plate motions. *Geophysical Journal International*, **181**, 1–80.

Fontijn, K., Rawson, H., Van Daele, M., Moernaut, J., Abarzúa, A.M., Heirman, K., Bertrand, S., Pyle, D.M., Mather, T.A., Batist, M. de, **Naranjo, J.-A.** and **Moreno, H.** (2016) Synchronisation of sedimentary records using tephra: A postglacial tephrochronological model for the Chilean Lake District. *Quaternary Science Reviews*, **137**, 234–254.

Goldfinger, C., Galer, S., Beeson, J., Hamilton, T., Black, B., Romsos, C., Patton, J., Nelson, C.H., Hausmann, R. and **Morey, A.** (2017) The importance of site selection, sediment supply, and hydrodynamics: A case study of submarine paleoseismology on the northern Cascadia margin, Washington USA. *Marine Geology*, **384**, 4–46.

Goldfinger, C., Nelson, H., Morey, A.E., Johnson, J.E., Patton, J.R., Karabanov, E., Gutiérrez-Pastor, J., Eriksson, A.T., Gràcia, E., Dunhill, G., Enkin, R.J., Dallimore, A. and **Vallier, T.** (2012) Turbidite Event History—Methods and Implications for Holocene Paleoseismicity of the Cascadia Subduction Zone. *U.S. Geological Survey Professional Paper*, 170.

Grabowski, R.C., Droppo, I.G. and **Wharton, G.** (2011) Erodibility of cohesive sediment: The importance of sediment properties. *Earth-Science Reviews*, **105**, 101–120.

Heifetz, E., Agnon, A. and **Marco, S.** (2005) Soft sediment deformation by Kelvin Helmholtz Instability: A case from Dead Sea earthquakes. *Earth and Planetary Science Letters*, **236**, 497–504.

Hibsch, C., Alvarado, A., Yepes, H., Perez, V.H. and **Sébrier, M.** (1997) Holocene liquefaction and soft-sediment deformation in Quito (Ecuador): A paleoseismic history recorded in lacustrine sediments. *Journal of Geodynamics*, **24**, 259–280.

Howarth, J.D., Fitzsimons, S.J., Norris, R.J. and **Jacobsen, G.E.** (2014) Lake sediments record high intensity shaking that provides insight into the location and rupture length of

large earthquakes on the Alpine Fault, New Zealand. *Earth and Planetary Science Letters*, **403**, 340–351.

Idini, B., Rojas, F., Ruiz, S. and **Pastén, C.** (2017) Ground motion prediction equations for the Chilean subduction zone. *Bull Earthquake Eng*, **15**, 1853–1880.

Ikehara, K., Kanamatsu, T., Nagahashi, Y., Strasser, M., Fink, H., Usami, K., Irino, T. and **Wefer, G.** (2016) Documenting large earthquakes similar to the 2011 Tohoku-oki earthquake from sediments deposited in the Japan Trench over the past 1500 years. *Earth and Planetary Science Letters*, **445**, 48–56.

Ikehara, K., Usami, K. and **Kanamatsu, T.** (2020) Repeated occurrence of surface-sediment remobilization along the landward slope of the Japan Trench by great earthquakes. *Earth Planets Space*, **72**, 1–9.

Jolly, R.J.H. and **Lonergan, L.** (2002) Mechanisms and controls on the formation of sand intrusions. *Journal of the Geological Society*, **159**, 605–617.

Jutzeler, M., White, J.D.L., Talling, P.J., McCanta, M., Morgan, S., Le Friant, A. and **Ishizuka, O.** (2014) Coring disturbances in IODP piston cores with implications for offshore record of volcanic events and the Missoula megafloods. *Geochem. Geophys. Geosyst.*, **15**, 3572–3590.

Kawase, H. (2003) 61 Site effects on strong ground motions. In: *International handbook of earthquake and engineering seismology* 937th ed., *International geophysics series*, **81**, pp. 1013–1030. Academic Press, London, San Diego, Calif.

Kioka, A., Schwestermann, T., Moernaut, J., Ikehara, K., Kanamatsu, T., McHugh, C.M., dos Santos Ferreira, C., Wiemer, G., Haghipour, N., Kopf, A.J., Eglinton, T.I. and **Strasser, M.** (2019) Megathrust earthquake drives drastic carbon supply to the hadal trench. *Scientific Reports*.

Knipe, R.J. (1986) Deformation mechanism path diagrams for sediments undergoing lithification. *Structural Fabric in Deep Sea Drilling Project Cores from Forearcs*, **166**, 151.

Krawcyzk, C. (2003) Amphibious seismic survey images plate interface at 1960 Chile Earthquake. *Eos Trans. AGU*, **84**, 301.

Kremer, K., Wirth, S.B., Reusch, A., Fäh, D., Bellwald, B., Anselmetti, F.S., Girardclos, S. and **Strasser, M.** (2017) Lake-sediment based paleoseismology: Limitations and perspectives from the Swiss Alps. *Quaternary Science Reviews*, **168**, 1–18.

Lazo, R.G. (2008), *ESTUDIO DE LOS DAÑOS DE LOS TERREMO TOS DEL 21 Y 22 DE MAYO DE 1960*.

Lomnitz, C. (1970) Major earthquakes and tsunamis in Chile during the period 1535 to 1955. *Geol Rundsch,* **59**, 938–960.

Lowe, D. (1975) Water escape structures in coarse-grained sediments. *Sedimentology*, **22**, 157–204.

Lowe, D.R. (1982) Sediment Gravity Flows: II Depositional Models with Special Reference to the Deposits of High-Density Turbidity Currents. *Journal of Sedimentary Research,* **Vol. 52**.

Lu, Y., Waldmann, N., Ian Alsop, G. and **Marco, S.** (2017) Interpreting Soft Sediment Deformation and Mass Transport Deposits as Seismites in the Dead Sea Depocenter. *J. Geophys. Res. Solid Earth,* **122**, 8305–8325.

Maltman, A., ed. (1994), *The Geological Deformation of Sediments*, Chapman & Hall, 368 pp.

Marco, S. and **Agnon, A.** (1995) Prehistoric earthquake deformations near Masada, Dead Sea graben. *Geology,* **23**, 695–698.

Marco, S., Stein, M., Agnon, A. and **Ron, H.** (1996) Long-term earthquake clustering: A 50,000-year paleoseismic record in the Dead Sea Graben. *J. Geophys. Res. Solid Earth,* **101**, 6179–6191.

McHugh, C.M., Kanamatsu, T., Seeber, L., Bopp, R., Cormier, M.-H. and **Usami, K.** (2016) Remobilization of surficial slope sediment triggered by the A.D. 2011 Mw9 Tohoku-Oki earthquake and tsunami along the Japan Trench. *Geology*, **44**, 391–394.

McHugh, C.M., Seeber, L., Rasbury, T., Strasser, M., Kioka, A., Kanamatsu, T., Ikehara, K. and **Usami, K.** (2020) Isotopic and sedimentary signature of megathrust ruptures along the Japan subduction margin. *Marine Geology*, 106283.

Meier, M.-A., Ampuero, J.P. and **Heaton, T.H.** (2017) The hidden simplicity of subduction megathrust earthquakes. *Science (New York, N.Y.),* **357**, 1277–1281.

Métois, M., Socquet, A. and **Vigny, C.** (2012) Interseismic coupling, segmentation and mechanical behavior of the central Chile subduction zone. *J. Geophys. Res.*, **117**.

Meunier, P., Hovius, N. and **Haines, J.A.** (2008) Topographic site effects and the location of earthquake induced landslides. *Earth and Planetary Science Letters,* **275**, 221–232.

Moernaut, J., Van Daele, M., Fontijn, K., Heirman, K., Kempf, P., Pino, M., Valdebenito, G., Urrutia, R., Strasser, M. and **Batist, M.** de (2018) Larger earthquakes recur more periodically: New insights in the megathrust earthquake cycle from lacustrine turbidite records in south-central Chile. *Earth and Planetary Science Letters,* **481**, 9–19.

Moernaut, J., Van Daele, M., Heirman, K., Fontijn, K., Strasser, M., Pino, M., Urrutia, R. and **Batist, M.** de (2014) Lacustrine turbidites as a tool for quantitative earthquake

reconstruction: New evidence for a variable rupture mode in south central Chile. *J. Geophys. Res. Solid Earth*, **119**, 1607–1633.

Moernaut, J., Van Daele, M., Heirman, K., Wiemer, G., Molenaar, A., Vandorpe, T., Melnick, D., Hajdas, I., Pino, M., Urrutia, R. and **Batist, M.** de (2019) The subaqueous landslide cycle in south-central Chilean lakes: The role of tephra, slope gradient and repeated seismic shaking. *Sedimentary Geology*, **381**, 84–105.

Moernaut, J., Van Daele, M., Strasser, M., Clare, M.A., Heirman, K., Viel, M., Cardenas, J., Kilian, R., Ladrón de Guevara, B., Pino, M., Urrutia, R. and **De Batist, M.** (2017) Lacustrine turbidites produced by surficial slope sediment remobilization. A mechanism for continuous and sensitive turbidite paleoseismic records. *Marine Geology*, **384**, 159–176.

Molenaar, A., Moernaut, J., Wiemer, G., Dubois, N. and **Strasser, M.** (2019) Earthquake Impact on Active Margins: Tracing Surficial Remobilization and Seismic Strengthening in a Slope Sedimentary Sequence. *Geophysical Research Letters*, **41**, 1195.

Monecke, K., Anselmetti, F.S., Becker, A., Sturm, M. and **Giardini, D.** (2004) The record of historic earthquakes in lake sediments of Central Switzerland. *Tectonophysics*, **394**, 21–40.

Moreno, M., Melnick, D., Rosenau, M., Baez, J., Klotz, J., Oncken, O., Tassara, A., Chen, J., Bataille, K., Bevis, M., Socquet, A., Bolte, J., Vigny, C., Brooks, B., Ryder, I., Grund, V., Smalley, B., Carrizo, D., Bartsch, M. and **Hase, H.** (2012) Toward understanding tectonic control on the Mw 8.8 2010 Maule Chile earthquake. *Earth and Planetary Science Letters*, **321-322**, 152–165.

Moreno, M.S., Bolte, J., Klotz, J. and **Melnick, D.** (2009) Impact of megathrust geometry on inversion of coseismic slip from geodetic data: Application to the 1960 Chile earthquake. *Geophysical Research Letters*, **36**, 589.

Musson, R.M.W., Grünthal, G. and **Stucchi, M.** (2010) The comparison of macroseismic intensity scales. *J Seismol*, **14**, 413–428.

Mutti, E. (1992), *Turbidite sandstones*, Agip, Istituto di geologia, Università di Parma.

Nelson Pulido, Yuji Yagi, Hiroyuki Kumagai and **Naoki Nishimura** (2011) Rupture process and coseismic deformations of the 27 February 2010 Maule earthquake, Chile. *Earth Planet Sp*, **63**, 955–959.

Noguchi, T., Tanikawa, W., Hirose, T., Lin, W., Kawagucci, S., Yoshida-Takashima, Y., Honda, M.C., Takai, K., Kitazato, H. and **Okamura, K.** (2012) Dynamic process of

turbidity generation triggered by the 2011 Tohoku-Oki earthquake. *Geochem. Geophys. Geosyst.,* **13**, Q11003.

Obermeier, S.F. (2009) Chapter 7 Using Liquefaction-Induced and Other Soft-Sediment Features for Paleoseismic Analysis. In: *Paleoseismology, International Geophysics,* **95**, pp. 497–564. Elsevier.

Ortner, H. (2007) Styles of soft-sediment deformation on top of a growing fold system in the Gosau Group at Muttekopf, Northern Calcareous Alps, Austria: Slumping versus tectonic deformation. *Sedimentary Geology,* **196**, 99–118.

Owen, G. (1987) Deformation processes in unconsolidated sands. *Geological Society, London, Special Publications,* **29**, 11–24.

Owen, G. (2003) Load structures: gravity-driven sediment mobilization in the shallow subsurface. *Geological Society, London, Special Publications,* **216**, 21–34.

Owen, G. and **Moretti, M.** (2011) Identifying triggers for liquefaction-induced soft-sediment deformation in sands. *Sedimentary Geology,* **235**, 141–147.

Owen, G., Moretti, M. and **Alfaro, P.** (2011) Recognising triggers for soft-sediment deformation: Current understanding and future directions. *Sedimentary Geology,* **235**, 133–140.

Pouderoux, H., Proust, J.-N. and **Lamarche, G.** (2014) Submarine paleoseismology of the northern Hikurangi subduction margin of New Zealand as deduced from Turbidite record since 16 ka. *Quaternary Science Reviews,* **84**, 116–131.

Rodrıguez-Pascua, M., Vicente, G. de, **Calvo, J.P.** and **Pérez-López, R.** (2003) Similarities between recent seismic activity and paleoseismites during the late miocene in the external Betic Chain (Spain): relationship by ‘b’value and the fractal dimension. *Journal of Structural Geology,* **25**, 749–763.

Rodríguez-Pascua, M.A., Garduño-Monroy, V.H., Israde-Alcántara, I. and **Pérez-López, R.** (2010) Estimation of the paleoepicentral area from the spatial gradient of deformation in lacustrine seismites (Tierras Blancas Basin, Mexico). *Quaternary International,* **219**, 66–78.

Rodríguez-Pascua, M.A., Calvo, J.P., Vicente, G. de and **Gómez-Gras, D.** (2000) Soft-sediment deformation structures interpreted as seismites in lacustrine sediments of the Prebetic Zone, SE Spain, and their potential use as indicators of earthquake magnitudes during the Late Miocene. *Sedimentary Geology,* **135**, 117–135.

Sawyer, D.E. and **DeVore, J.R.** (2015) Elevated shear strength of sediments on active margins: Evidence for seismic strengthening. *Geophysical Research Letters*, **42**, 10,216-10,221.

Schindelin, J., Arganda-Carreras, I., Frise, E., Kaynig, V., Longair, M., Pietzsch, T., Preibisch, S., Rueden, C., Saalfeld, S., Schmid, B., Tinevez, J.-Y., White, D.J., Hartenstein, V., Eliceiri, K., Tomancak, P. and **Cardona, A.** (2012) Fiji: an open-source platform for biological-image analysis. *Nature methods*, **9**, 676–682.

Schwestermann, T., Huang, J., Konzett, J., Kioka, A., Wefer, G., Ikehara, K., Moernaut, J., Eglinton, T.I. and **Strasser, M.** (2020) Multivariate Statistical and Multiproxy Constraints on Earthquake-Triggered Sediment Remobilization Processes in the Central Japan Trench. *Geochem. Geophys. Geosyst.*, **21**.

Sims, J.D. (1973) Earthquake-induced structures in sediments of van Norman lake, san fernando, california. *Science (New York, N.Y.)*, **182**, 161–163.

Tassara, A., Götze, H.-J., Schmidt, S. and **Hackney, R.** (2006) Three-dimensional density model of the Nazca plate and the Andean continental margin. *J. Geophys. Res.*, **111**.

U.S. Geological Survey (2020), *M 8.8 - offshore Bio-Bio, Chile.* https://earthquake.usgs.gov/earthquakes/eventpage/official20100227063411530_30/executive. Accessed December 5, 2020.

Üner, S., Özsayın, E. and **Selçuk, A.S.** (2019) Seismites as an indicator for determination of earthquake recurrence interval: A case study from Erciş Fault (Eastern Anatolia-Turkey). *Tectonophysics*, **766**, 167–178.

Van Daele, M., Moernaut, J., Doom, L., Boes, E., Fontijn, K., Heirman, K., Vandoorne, W., Hebbeln, D., Pino, M., Urrutia, R., Brümmer, R., Batist, M. de and **Trofimovs, J.** (2015) A comparison of the sedimentary records of the 1960 and 2010 great Chilean earthquakes in 17 lakes. Implications for quantitative lacustrine palaeoseismology. *Sedimentology*, **62**, 1466–1496.

Van Daele, M., Moernaut, J., Silversmit, G., Schmidt, S., Fontijn, K., Heirman, K., Vandoorne, W., Clercq, M. de, **van Acker, J., Wolff, C., Pino, M., Urrutia, R., Roberts, S.J., Vincze, L.** and **Batist, M.** de (2014) The 600 yr eruptive history of Villarrica Volcano (Chile) revealed by annually laminated lake sediments. *Geological Society of America Bulletin*, **126**, 481–498.

Wetzler, N., Marco, S. and **Heifetz, E.** (2010) Quantitative analysis of seismogenic shear-induced turbulence in lake sediments. *Geology*, **38**, 303–306.

Wiegel, R.L. (1964) Tsunamis, storm surges, and harbor oscillations. *Oceanographical Engineering*, 95–127.

Wiemer, G. and **Kopf, A.** (2017) Influence of diatom microfossils on sediment shear strength and slope stability. *Geochem. Geophys. Geosyst.*, **18**, 333–345.

Wils, K., Van Daele, M., Kissel, C., Moernaut, J., Schmidt, S., Siani, G. and **Lastras, G.** (submitted) Seismo-turbidites in Aysén Fjord (Southern Chile) Reveal a Complex Pattern of Rupture Modes Along the 1960 Megathrust Earthquake Segment. *Journal of Geophysical Research*.

Preprint manuscript: submitted to Sedimentology on 17.08.2020 (Molenaar et al.)

Supporting Information for

What Controls the Remobilization and Deformation of Surficial Sediment by Seismic Shaking? Linking Lacustrine Slope Stratigraphy to Great Earthquakes in South-Central Chile

Ariana Molenaar[1], Maarten Van Daele[2], Thomas Vandorpe[3], Gerald Degenhart[1,4], Marc De Batist[2], Roberto Urrutia[5], Mario Pino[6], Michael Strasser[1], Jasper Moernaut[1]

[1]Institute of Geology, University of Innsbruck, Innsbruck, Austria, [2] Renard Centre of Marine Geology, Ghent University, Ghent, Belgium, [3] Flanders Marine Institute (VLIZ), Oostende, Belgium, [4] Medical University Innsbruck, Innsbruck, Austria, [5] Faculty of Environmental Sciences & EULA-Center, University of Concepción, Barrio Universitario s/n, Concepción, Chile, [6] Inst. Ciencias de la Tierra & Transdisciplinary Center for Quaternary Research in the South of Chile, Universidad Austral de Chile, Valdivia, Chile

File Content

Figures S1-S12

Introduction

This supporting informtion contains bathymetric maps and slope maps for lake Riñihue (Figure S1) and lake Calafquén (Figure S2); reference basin core correlation to a dated seismo-turbidite record (Figure S3-S4); soft sediment deformation structure (SSDS) identification for the reference basin cores (Figure S5) and slope-to-basin core correlation for lake Riñihue (Figure S6-S8) and Lago Calafquén (S9-S11); density data for two lake Riñihue and two lake Calafquén cores (Figure S12).

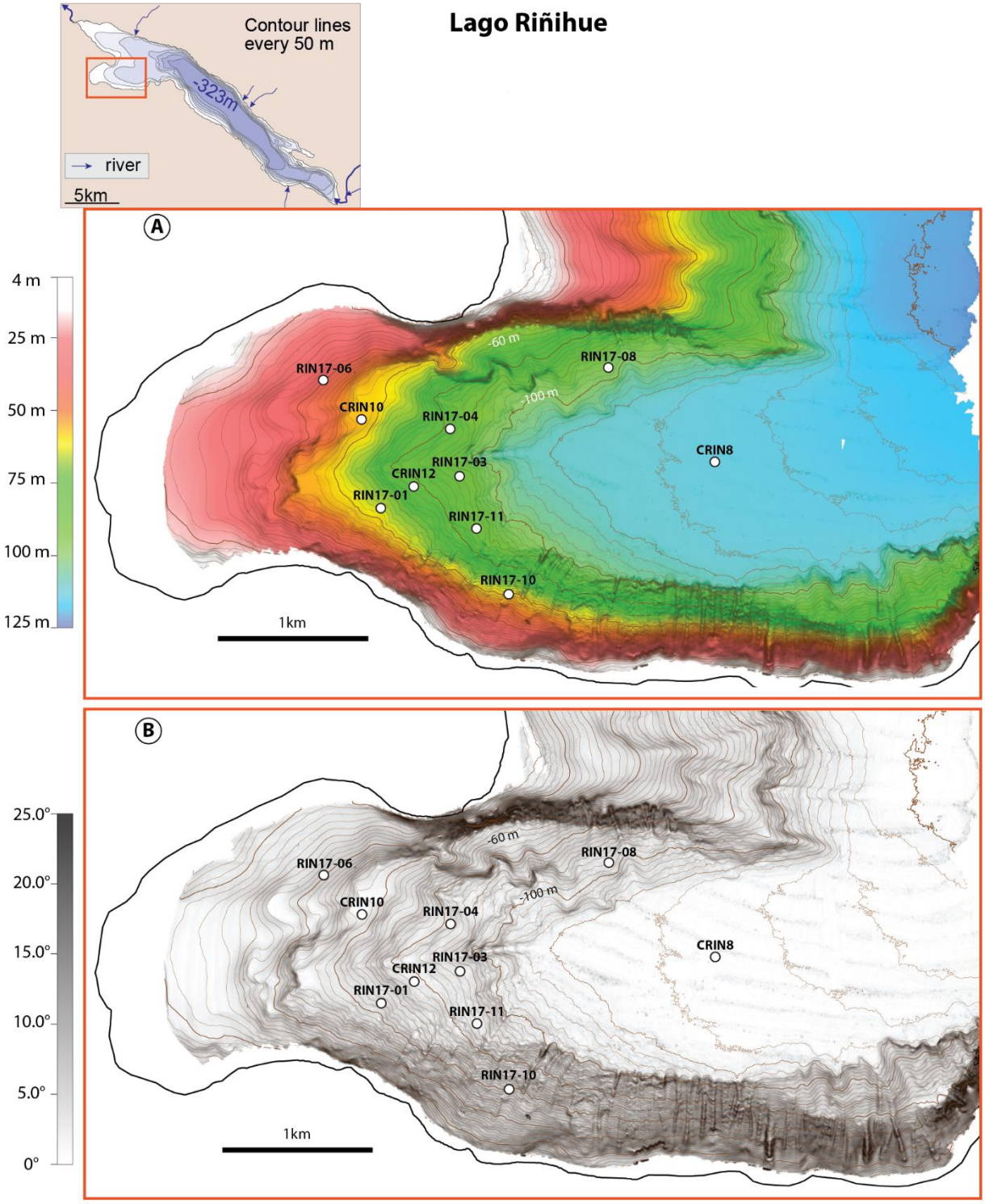

Figure S14 Lake Riñihue: Overview map of the complete lake adapted from Moernaut et al. (2014) and A) bathymetric map as well as B) slope angle map. Contour line distance is 2 m.

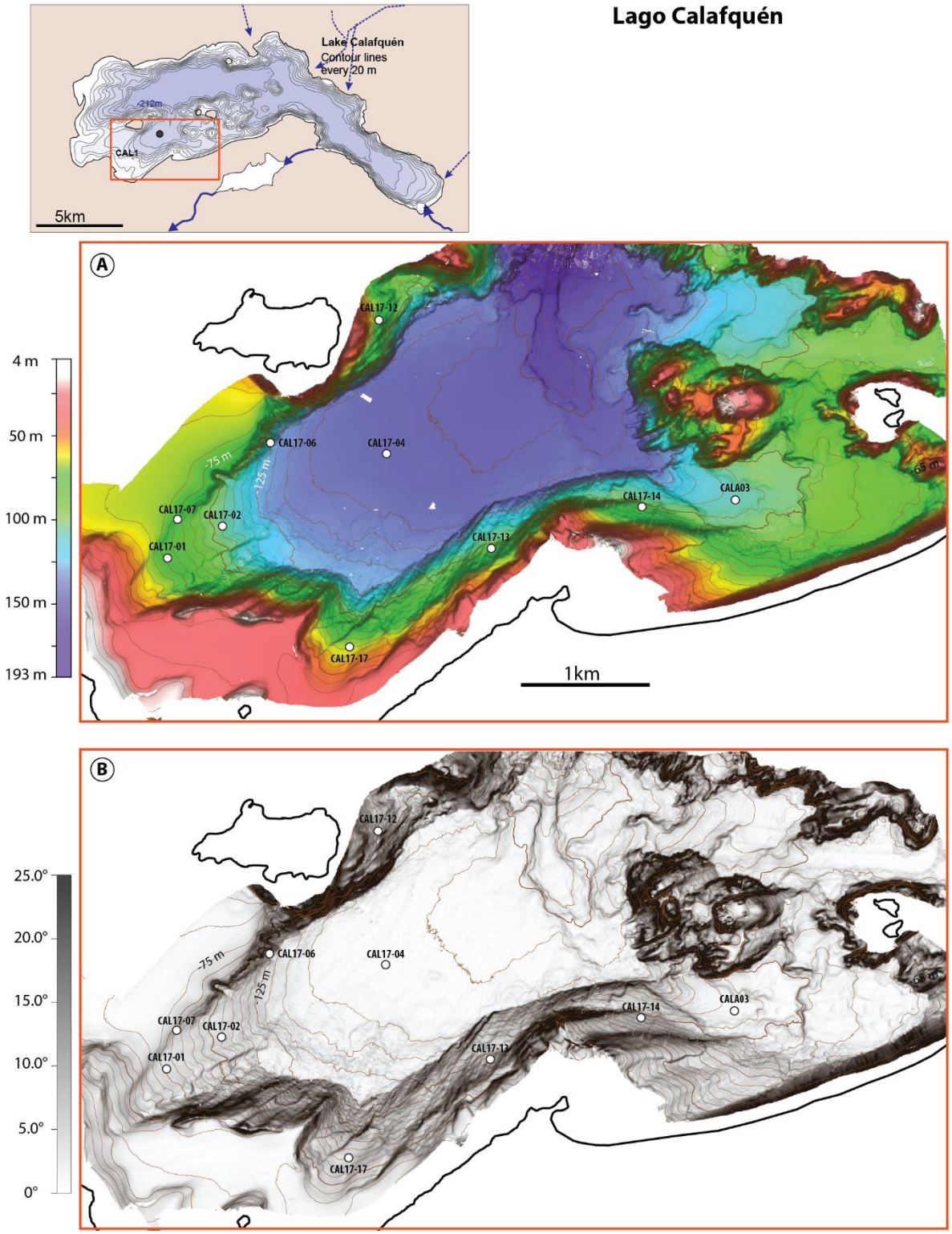

Figure S2 Lake Calafquén: Overview map of the complete lake adapted from Moernaut et al. (2014) and A) bathyetric map as well as B) slope angle map. Data already presented in Moernaut et al. (2019). Contour line distance is 5 m.

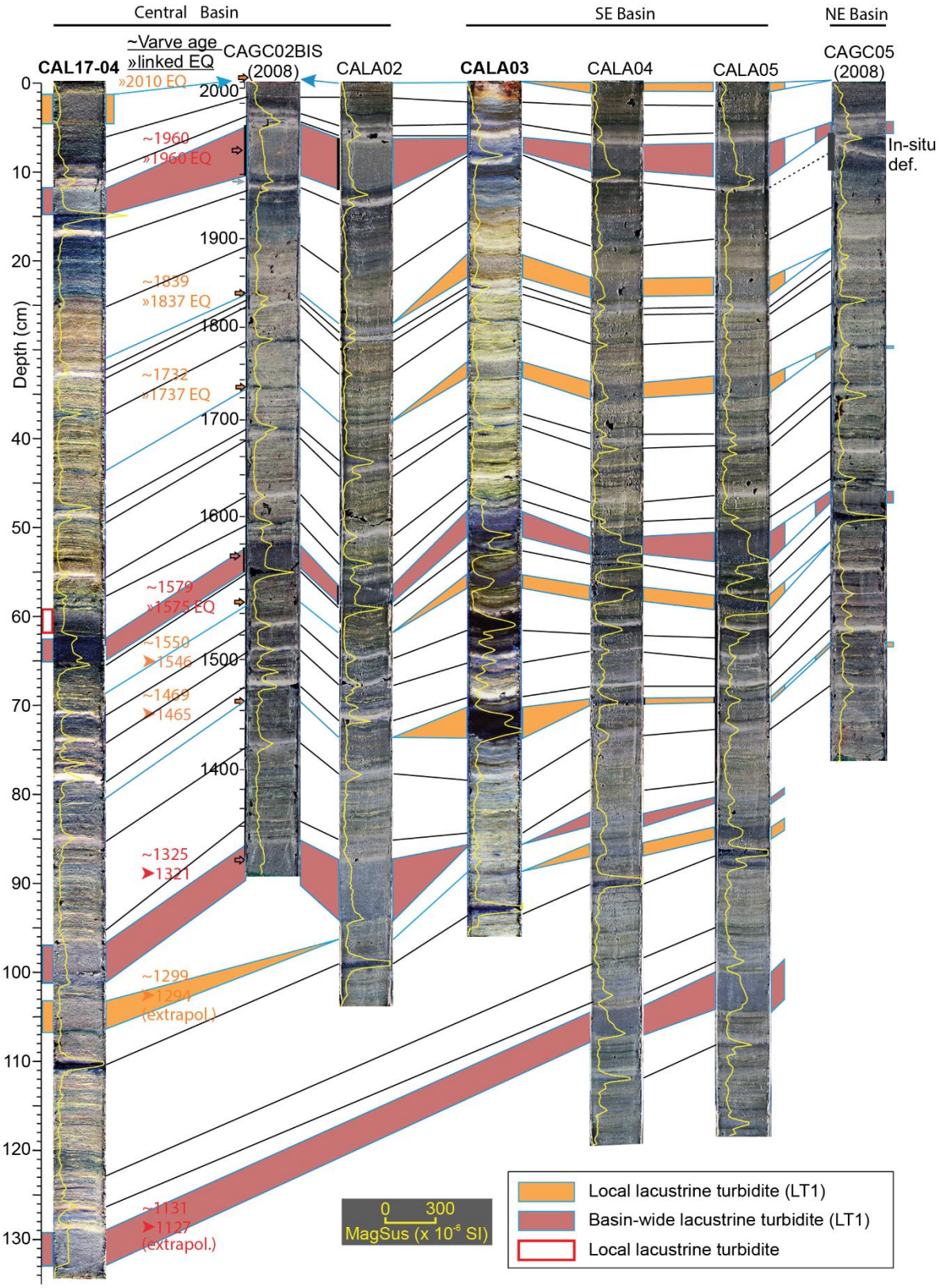

Figure S3 Basin core correlation of reference basin cores CAL17-04 and CALA03 to cores and age-depth model as published by Moernaut et al. (2014).

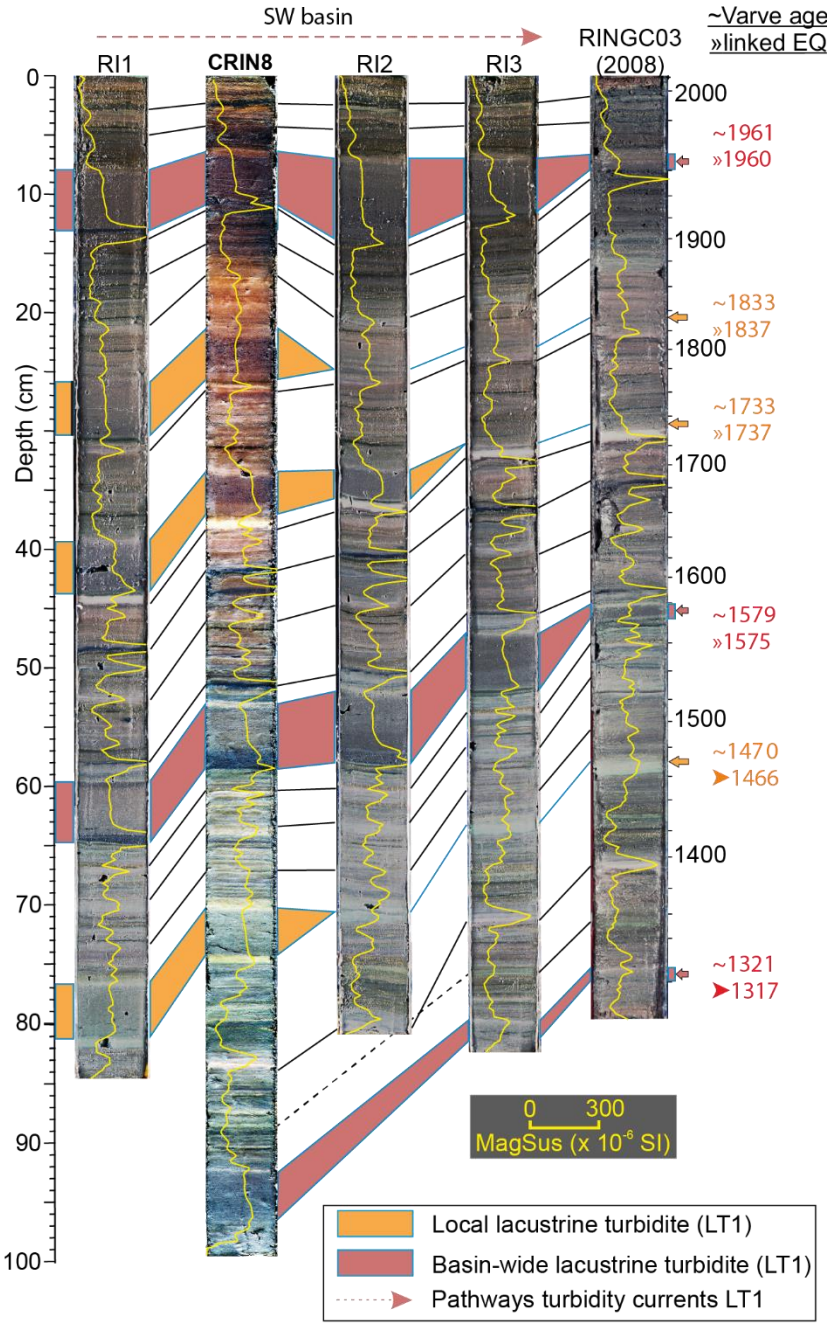

Figure S4 Basin core correlation of reference basin core CRIN8 to cores and age-depth model as published by Moernaut et al. (2014).

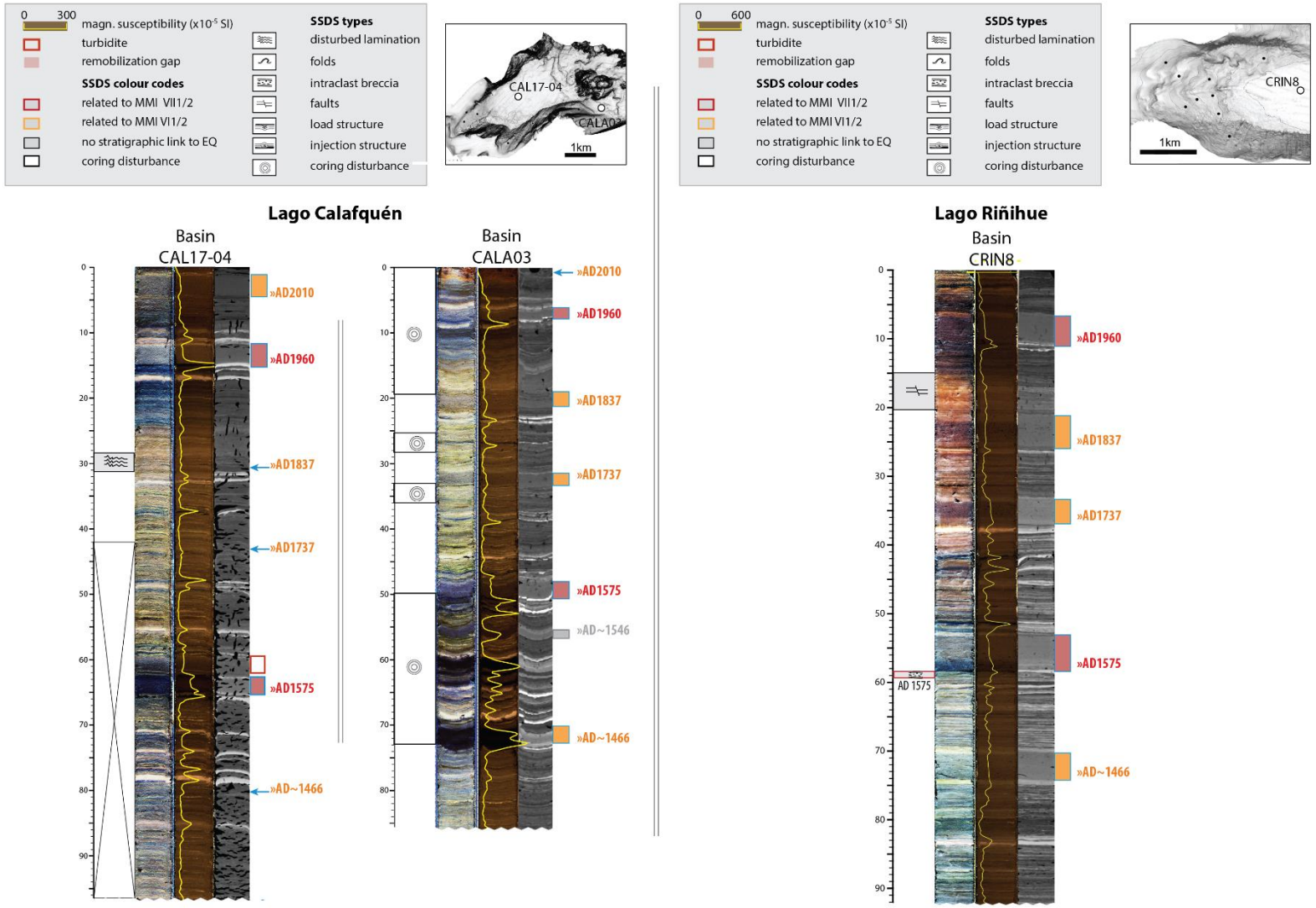

Figure S5 SSDS identification in the reference basin cores of lake Calafquén and Lago Riñihue. For each core:Left image is histogram equalized image, middle is image taken by ITRAX XRF scanner with polarizing filter and right is medical CT image. Black spots in CT image are degassing cracks.

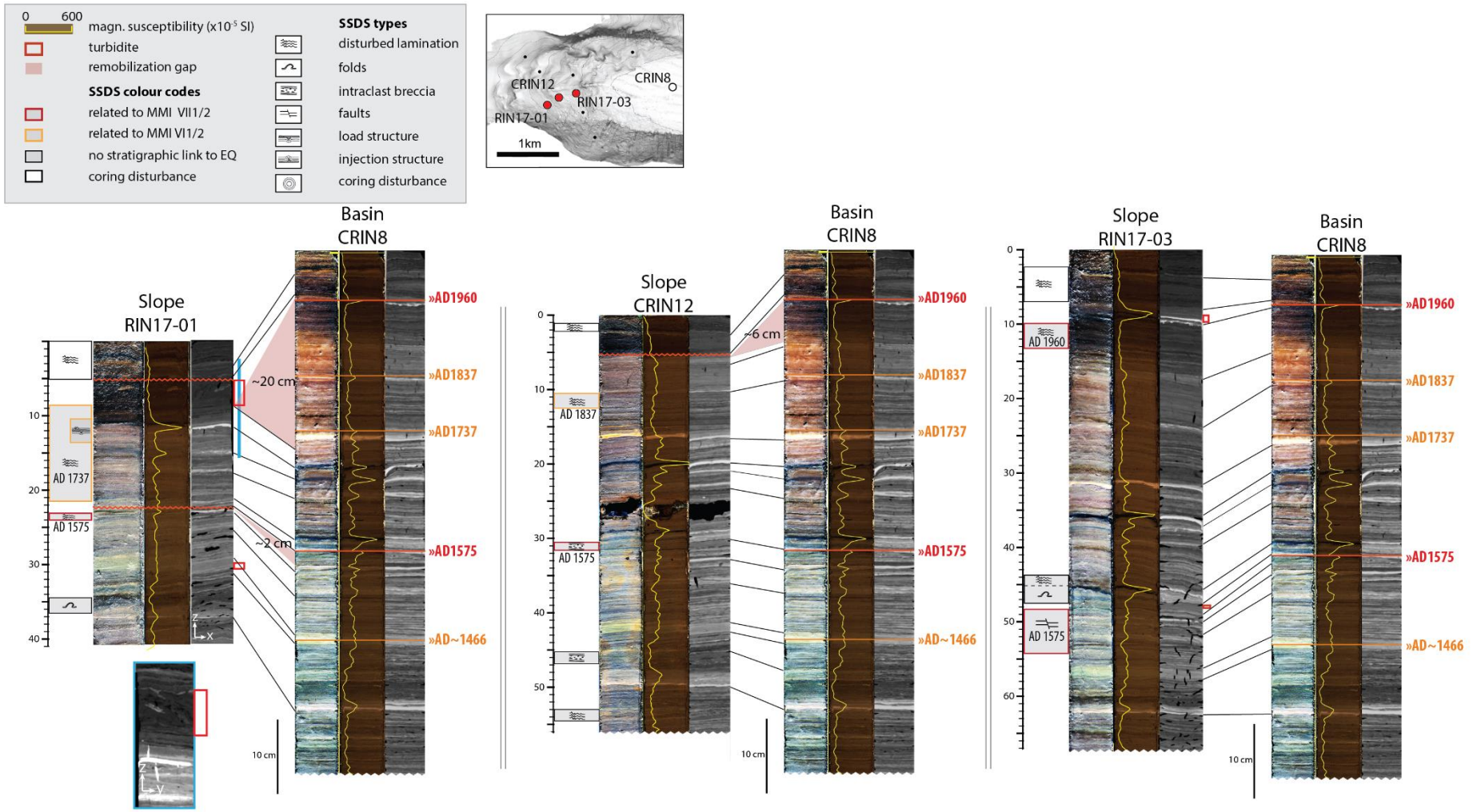

Figure S15 South-western slope-to-basin core correlations for lake Riñihue. For each core: Left image is histogram equalized image, middle is image taken by ITRAX XRF scanner with polarizing filter and right is medical CT image. Black spots in CT image are degassing cracks.

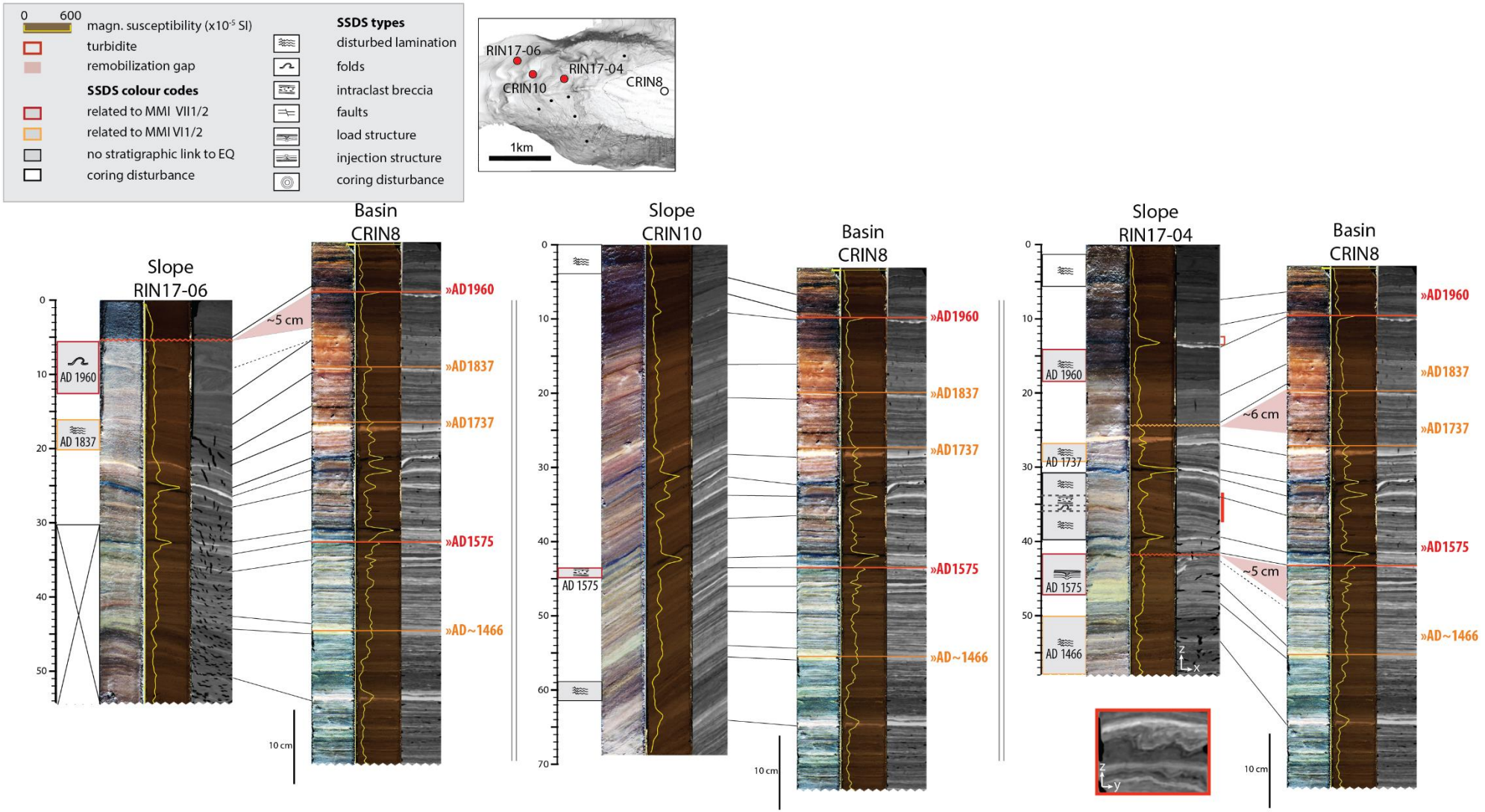

Figure S7 North-western slope-to-basin core correlations for lake Riñihue. For each core: Left image is histogram equalized image, middle is image taken by ITRAX XRF scanner with polarizing filter and right is medical CT image. Black spots in CT image are degassing cracks.

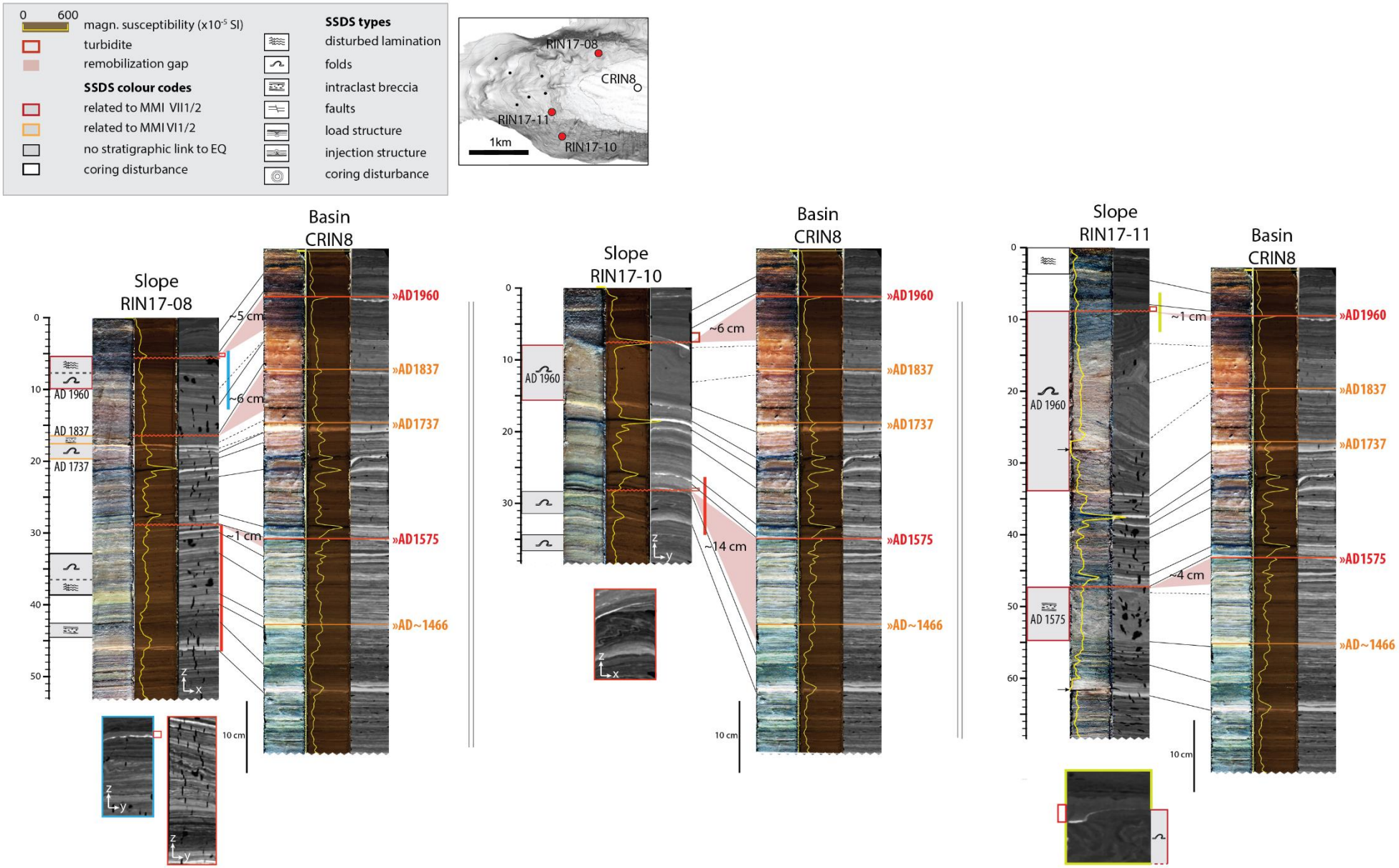

Figure S8 Southern and northern slope to basin core correlations of lake Riñihue. For each core: Left image is histogram equalized image, middle is image taken by ITRAX XRF scanner with polarizing filter and right is medical CT image. Black spots in CT image are degassing cracks.

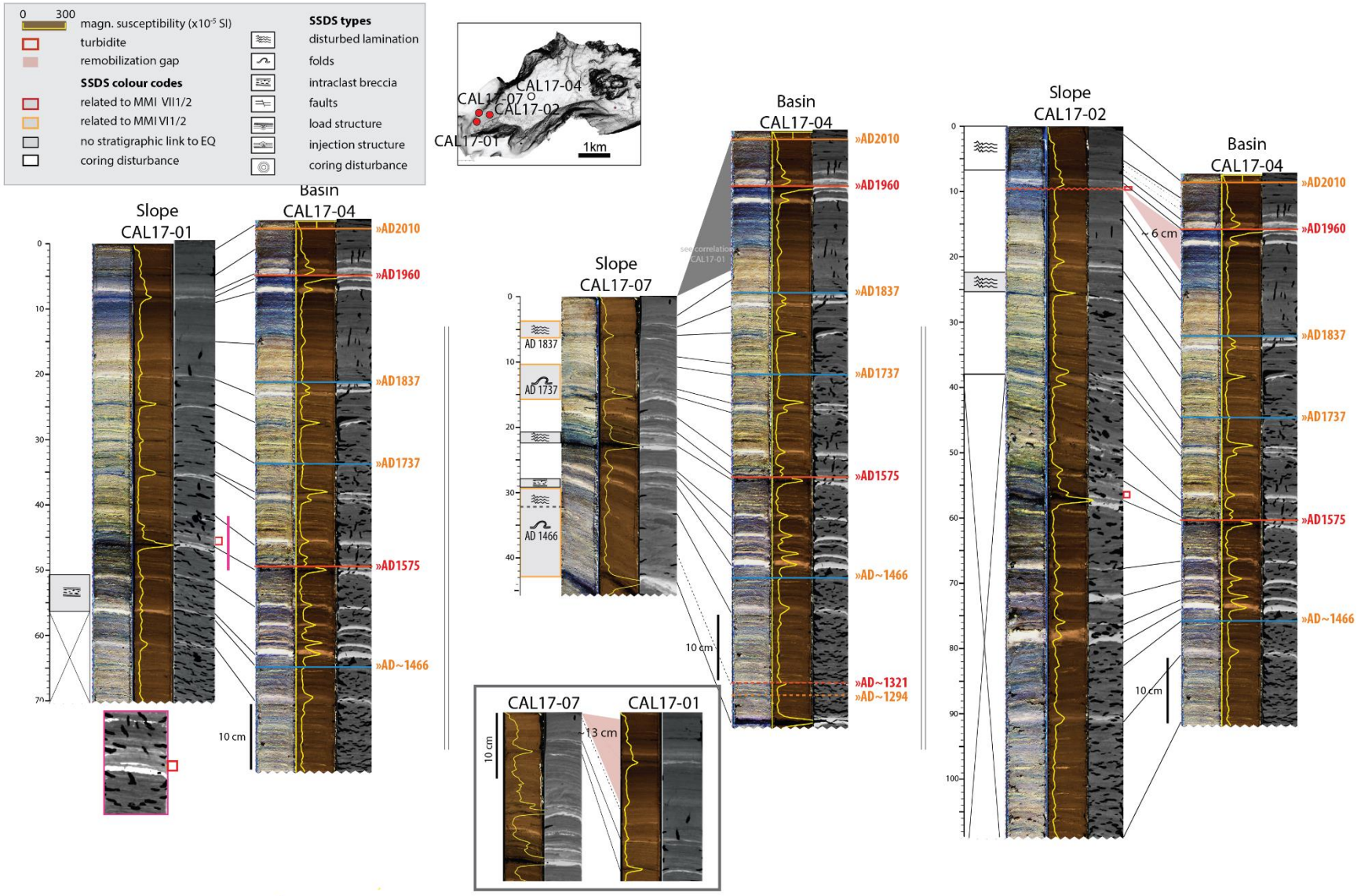

Figure S9 Western slope-to-basin core correlations of lake Calafquén. For each core: Left image is histogram equalized image, middle is image taken by ITRAX XRF scanner with polarizing filter and right is medical CT image. CAL17-07 is correlated to intact slope core CAL17-01. Black spots in CT image are degassing cracks.

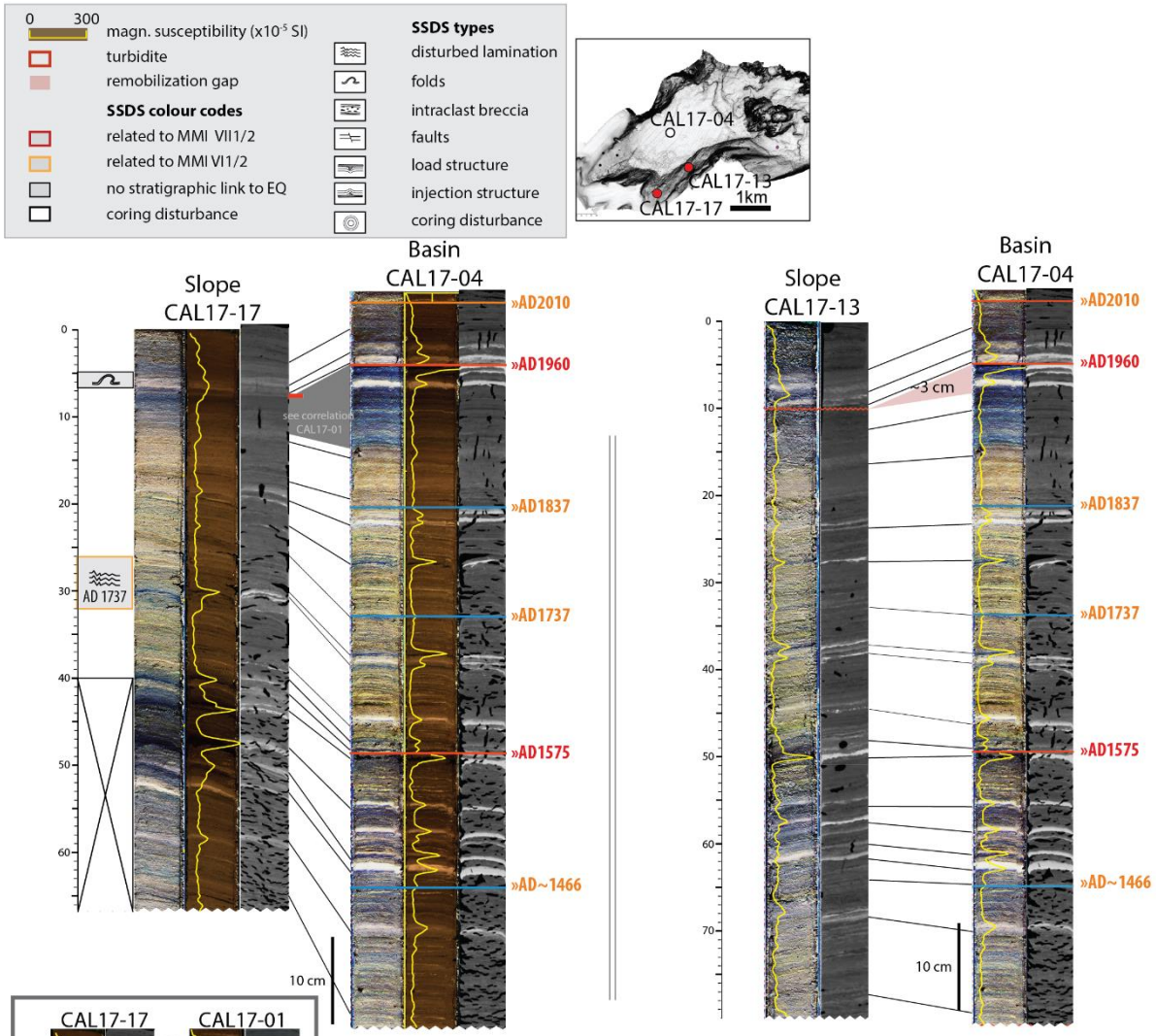

Figure S10 Southern slope-to-basin core correlations of lake Calafquén. For each core: Left image is histogram equalized image, middle is image taken by ITRAX XRF scanner with polarizing filter and right is medical CT image. CAL17-17 is correlated to intact slope core CAL17-01. Black spots in CT image are degassing cracks.

Preprint manuscript: submitted to Sedimentology on 17.08.2020 (Molenaar et al.)

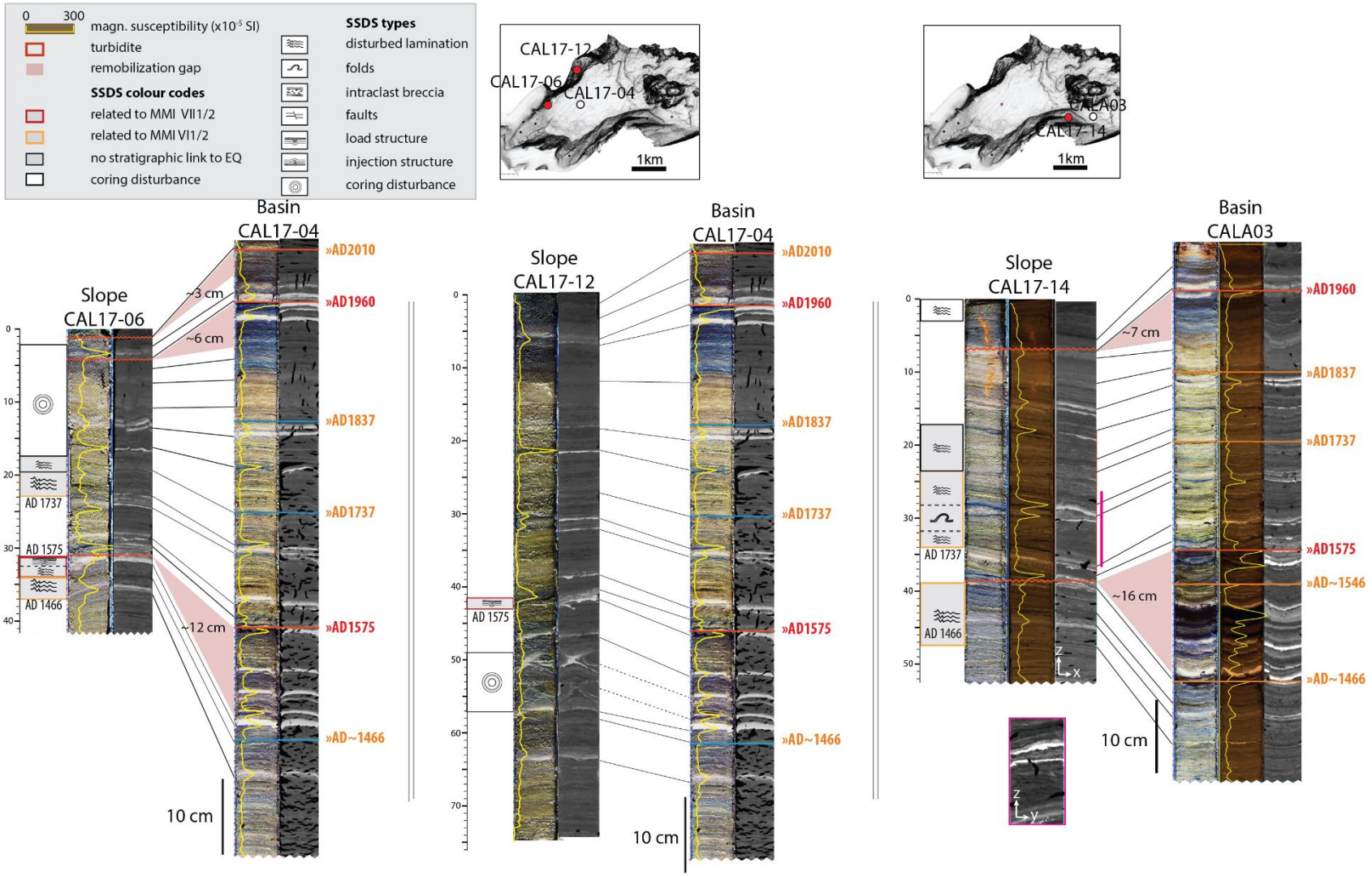

Figure S11 Northern and eastern basin slope-to-basin core correlations of lake Calafquén. For each core: Left image is histogram equalized image, middle is image taken by ITRAX XRF scanner with polarizing filter and right is medical CT image. Black spots in CT image are degassing cracks.

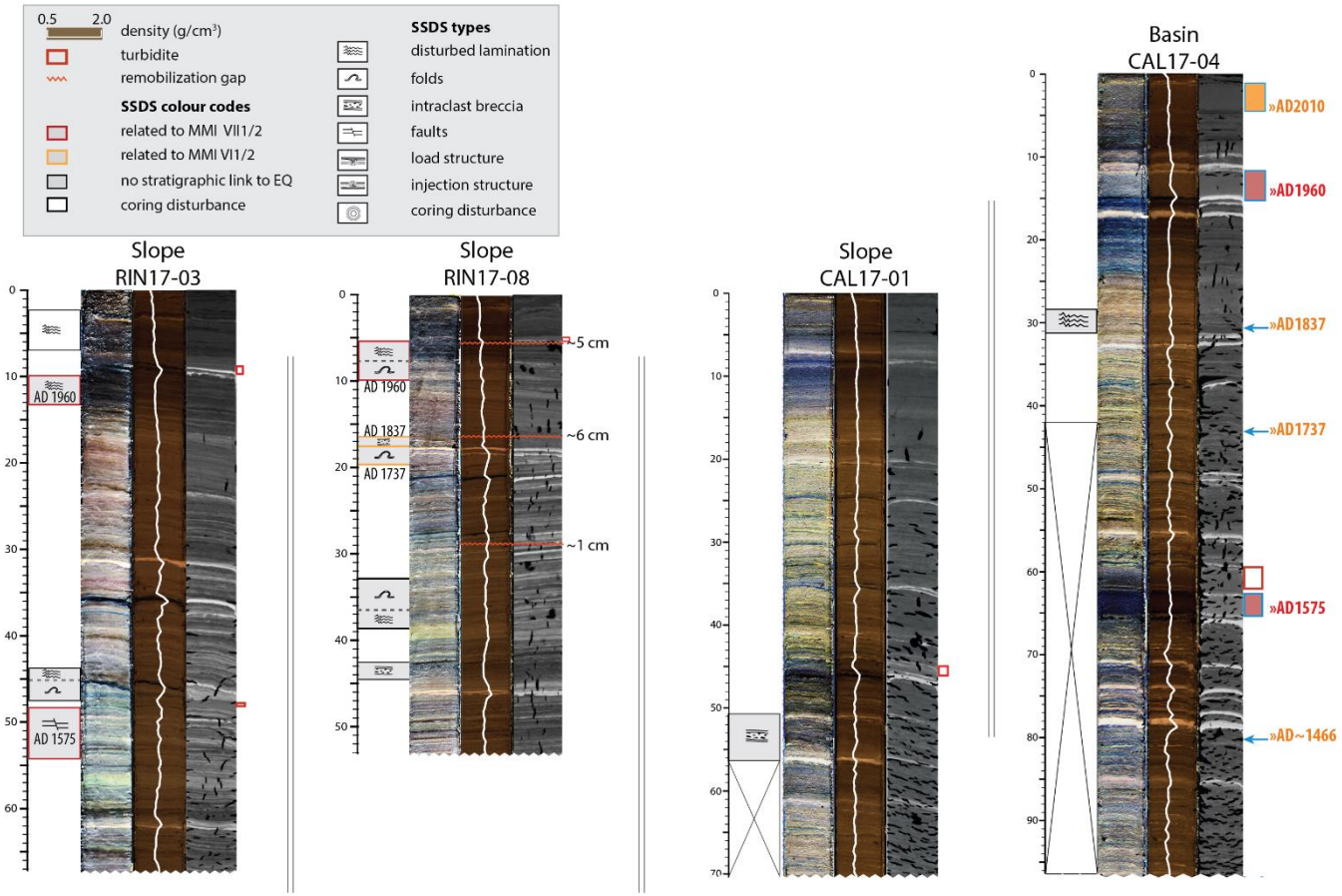

Figure S12 Two lake Riñihue (RIN17-03 and RIN17-08) and two lake Calafquén (CAL17-01 and CAL17-04) cores with gamma density data (white) as acquired by Geotek multi-sensor core logger. For each core: Left image is histogram equalized image, middle is image taken by ITRAX XRF scanner with polarizing filter and right is medical CT image. Black spots in CT image are degassing cracks.